Evaluation of Energy Consumption and Motion Accuracy for Underwater Gliders Based on Quadrant Analysis

Yang Song [a, b, c, 1], Weichao Shi [c, 1], Yanhui Wang [a, d, *], Hongyu Wu [e], Shaoqiong Yang [a, d], Hongbo Hou [b], Yunxin Xu [b]

[a] Key Laboratory of Mechanism Theory and Equipment Design of Ministry of Education, School of Mechanical Engineering, Tianjin University, Tianjin, 300350, China
[b] Department of Naval Architecture, Ocean and Marine Engineering, Faculty of Engineering, University of Strathclyde, Glasgow, G4 0LZ, UK
[c] Marine, Offshore and Subsea Technology Group, Mechanical Engineering and Marine Technology, School of Engineering, Newcastle University, NE1 7RU, UK
[d] The Joint Laboratory of Ocean Observing and Detection, Pilot National Laboratory for Marine Science and Technology, Qingdao, Shandong, 266237, China
[e] State Key Laboratory of Tribology in Advanced Equipment, Department of Mechanical Engineering, Tsinghua University, Beijing 100084, PR China

* Corresponding author. Key Laboratory of Mechanism Theory and Equipment Design of Ministry of Education, School of Mechanical Engineering, Tianjin University, Tianjin, 300350, China. E-mail address: yanhuiwang@tju.edu.cn (Y. Wang).

[1] Contributed equally to this work.

Abstract

Underwater gliders are well known as a type of enduring platform for underwater exploration; nevertheless, they have also been criticised in terms of their compromised course-keeping capability, particularly in harsh ocean environments. A motion controller that can improve motion accuracy while maintaining a low energy demand is preferred by developers and operators. In this paper, a motion controller based on a combined feedforward and Linear Quadratic Regulator (LQR) control is proposed. The controller has been evaluated in terms of energy consumption and motion accuracy with a fully coupled numerical model integrating the vehicle dynamics, the energy consumption and the control system. A energy-accuracy chart and a quadrant analysis are then introduced to support the analysis of the controller performance and the identification of the optimum operating conditions. Based on the prototype underwater glider that has been developed at Tianjin University, various case studies in different ocean environmental conditions are performed. The results show that the method proposed can quantitatively evaluate the performance of the vehicle to effectively achieve the balance between energy consumption and motion accuracy which can support the decision-making process for the best operation strategy.

Keywords: Underwater glider; Energy consumption model; Motion accuracy evaluation; LQR control; Quadrant Analysis

This is a peer-reviewed, accepted author manuscript of the following research article: Song, Y., Shi, W., Wang, Y., Wu, H., Yang, S., Hou, H., & Xu, Y. (2023). Evaluation of energy consumption and motion accuracy for underwater gliders based on quadrant analysis. *Ocean Engineering*, *285*, [115399]. https://doi.org/10.1016/j.oceaneng.2023.115399

1 Introduction

Ocean exploration plays an essential role in our sustainable development. The Autonomous Underwater Vehicle (AUV) has become one of the most important tools to better understand the ocean (Su and Wang, 2022). As a unique type of AUV, the underwater glider was initially proposed by Stommel in 1989 (Stommel, 1989). After 30+ years of continuous development, it has now been widely used for long-term, large-scale ocean observation and exploitation. At present, representative underwater gliders include Slocum (Webb et al., 2001), Seaglider (Eriksen et al., 2001), Spray (Sherman et al., 2001), SexExplorer (Field et al., 2015), and Petrel (Wang et al., 2011). Driven by the buoyancy force and combined with the hydrodynamic lifting forces on the wings, the underwater glider can perform sawtooth-like or spiral-like motion through the water column, as shown in Fig. 1. This unique and energy-efficient gliding motion enables underwater gliders to undertake endurance missions spanning thousands of kilometers and lasting several months (Ramos et al., 2018).

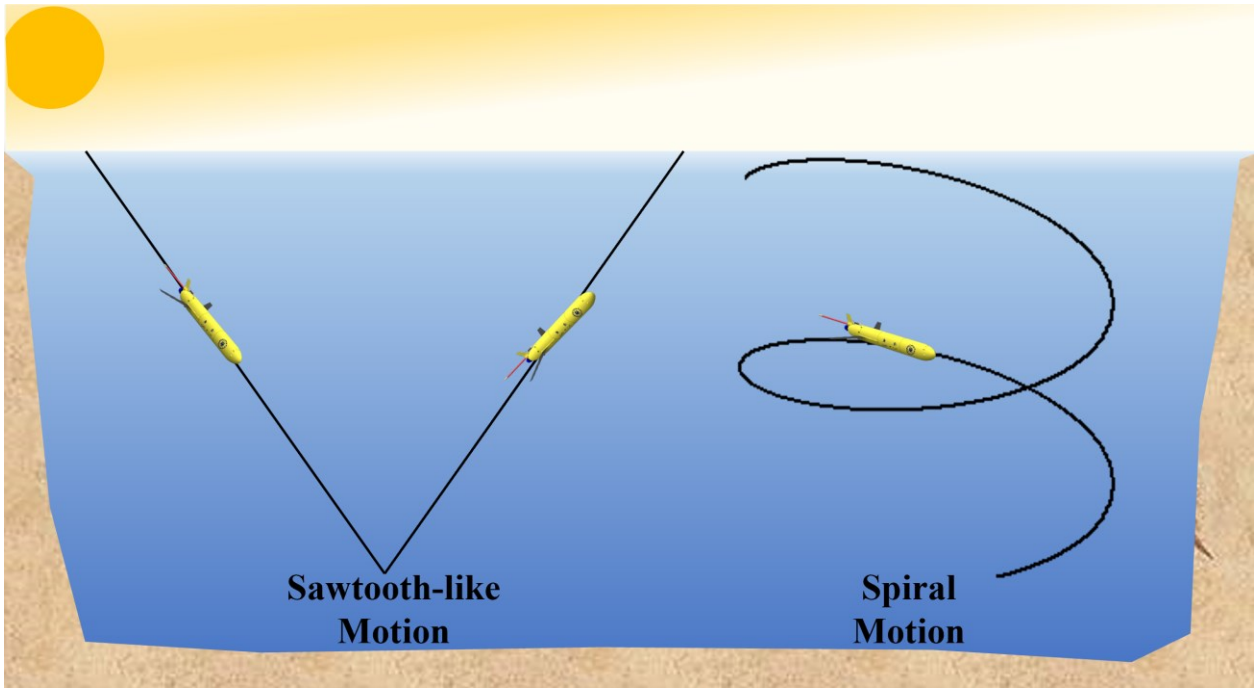

Fig. 1. Sawtooth-like and spiral motion of an underwater glider.

However, underwater gliders have often been criticised to compromise in terms of position accuracy. The reasons are manifold. Mostly it is due to the lack of underwater localisation systems. However, due to the nature of the gliding motion, underwater gliders are easily subjected to the disturbance of the ocean environment, which often results in drifting away with the currents, appearing in unwanted locations or confusing the measured data. This prevents the underwater gliders from being used to perform position accurate measurements. One potential solution to address this issue is to enhance the motion accuracy of underwater gliders while utilizing GPS data during surfacing to correct the position. However, this approach comes at the cost of significantly increased energy consumption.

While there have been advancements in thermal energy devices for underwater gliders (Falcão Carneiro and Gomes de Almeida, 2016, 2018; Ma et al., 2016), battery-powered underwater gliders remain the most widely used. To better understand energy consumption and improve the energy efficiency of battery-powered underwater gliders, several energy consumption models have been developed. Yu et al. (Yu et al., 2013) established an energy consumption model based on steady-state glider motion in the vertical plane. Then the model was extended to 3D space and described in detail in

(Cao et al., 2016b) and (Song et al., 2020). However, these studies did not consider the impact of environmental conditions and control systems on energy consumption. To address this, Song et al. (Song et al., 2021a) developed an energy consumption model for underwater gliders based on the least squares support vector machine. Despite encompassing numerous complex factors that are difficult to describe, this model fails to establish a clear relationship between these factors and energy consumption. Following this study, new energy consumption models considering ocean currents, seawater density variation and other control parameters are developed (Song et al., 2021b; Wu et al., 2021a, b). Recently, Sun et al. (Sun et al., 2023) optimized the internal layout of the blended-wing-body underwater glider using an energy consumption model. Wang et al. (Wang et al., 2023) integrated our previous energy consumption model (Song et al., 2020) into the virtual prototype technology to analyse the performance of the underwater glider. Based on the same energy consumption model, Wu et al, (Wu et al., 2023) investigated the energy efficiency of the underwater glider with the control parameters generated by a hybrid polynomial-based optimization method. Nevertheless, in the above studies, the energy consumption integrating the control systems has not been investigated, despite the significant impact that motion control systems have on energy consumption. Only recently, Wu et al. developed an energy consumption model considering the feedback control system and optimised the control parameters (Wu et al., 2021a, 2022). However, the energy consumption due to the feedback control is only analysed qualitatively.

On the other hand, various control strategies for underwater gliders have been developed in recent years, as summarized and reviewed in (Ullah et al., 2015; Wang et al., 2022). Among the various controllers, proportional–integral–derivative (PID) controller and Linear Quadratic Regulator (LQR) are the most commonly applied. Compared to the PID controller, the LQR is designed with a specific optimization objective to minimize a quadratic cost function. It is capable of finding optimal control inputs that minimize overall system performance criteria, including state error and energy usage, which aligns well with the purpose of this study. Furthermore, it has been demonstrated that the LQR outperforms the PID controller in glider system control (Noh et al., 2011). Therefore, in this study, the LQR is chosen instead of the PID controller, which requires complex manual tuning. Although the motion accuracy of the underwater gliders under the LQR control has been analysed (Cao et al., 2016a; Isa et al., 2014; Jantapremjit et al., 2020; Joo and Qu, 2015; Tchilian et al., 2017; Ullah et al., 2018; Wang et al., 2009), the energy consumption under LQR control has not been studied before, which remains as an unknown question.

In summary, the current evaluation and quantification of energy consumption and motion accuracy under feedback control for underwater gliders are insufficient. This deficiency results in inaccurate estimations of energy consumption, often leading to excessive energy usage. Consequently, it becomes challenging to assess the performance of the controller and make well-informed decisions to enable energy-efficient movements with high precision for underwater gliders.

A dynamics model serves as the foundation for energy prediction and motion analysis. Various methods, such as the Newton-Euler method (Leonard and Graver, 2001) and the Lagrange equation (Fan and Woolsey, 2014), have been adopted to establish the dynamics equations for underwater gliders. Ocean environments such as seawater density variation and current are considered in some dynamics euqations (Song et al., 2021b; Yang et al., 2017). Recently, data-driven environmental compensation models and multisource information fusion-based environment perception dynamics models have been proposed to reduce the prediction motion error in underwater gliders (Jing et al., 2022; Lei et al., 2023).

Motivated by the above problem and inspired by the existing methods, a vehicle dynamics model for underwater gliders is established to simulate the forces and motions of the vehicle. The model takes into account real ocean conditions, including seawater density gradient and ocean current. Subsequently, a motion controller comprising feedforward control and LQRs in the vertical and horizontal planes, respectively, is designed and integrated with the linearized dynamics model. The energy consumption

model and the motion accuracy evaluation method are proposed and implemented. Based on this, a quadrant chart is introduced to describe the performance of the controller on energy consumption and motion accuracy. Finally, taking the Petrel-II glider as the reference glider, case studies are performed with various ocean conditions to evaluate the performance of the LQR controller to be applied onto the Petrel-II glider and to illustrate the use of the developed quadrant analysis method.

The following contents of this paper are organized as follows. In Section 2, the dynamics model of an underwater glider is established. Following this, in Section 3 the dynamics model is linearized, and the controller based on feedforward and LQR is developed. Then the energy consumption, motion accuracy evaluation method and quadrant chart are proposed in Section 4. The case studies are performed and results are discussed in Section 5, followed by the illustration of the quadrant analysis methodology. Finally, Section 5 summarizes the main conclusions of this paper.

2 Dynamics model of underwater gliders

2.1 Reference frames and kinematic equations

As illustrated in Fig. 2, an inertial frame I_0 ($\boldsymbol{i}_1$, $\boldsymbol{i}_2$, $\boldsymbol{i}_3$) is defined as the tangent plane on the water surface to describe the position and orientation of a glider. The origin of I_0 is fixed at the starting point of the glider. The $\boldsymbol{i}_1$, $\boldsymbol{i}_2$ and $\boldsymbol{i}_3$ are unit vectors, which point towards the north, east and downwards normal to the earth's surface, respectively. Then, a body frame B_0 ($\boldsymbol{b}_1$, $\boldsymbol{b}_2$, $\boldsymbol{b}_3$) is established to describe the motion of a glider. The body frame moves with the glider. In this paper, the origin of B_0 is fixed at the centre of buoyancy of the glider, since the centre of gravity for gliders is constantly moving due to ballasting and de-ballasting and the vehicle control. The $\boldsymbol{b}_1$, $\boldsymbol{b}_2$ and $\boldsymbol{b}_3$ are unit vectors, which represent the longitudinal axis (directed from aft to fore), transversal axis (directed to starboard) and normal axis (directed from top to bottom), respectively. The dynamics equations and control strategies will be expressed with respect to the body frame. To perform the hydrodynamic calculations, a flow frame C_0 ($\boldsymbol{c}_1$, $\boldsymbol{c}_2$, $\boldsymbol{c}_3$) is also defined. The origin C_0 coincides with B_0 and the $\boldsymbol{c}_1$ axis points directly into the relative flow by rotating the body frame by an angle of attack α and a sideslip angle β, which will be further elaborated in Section 2.4.

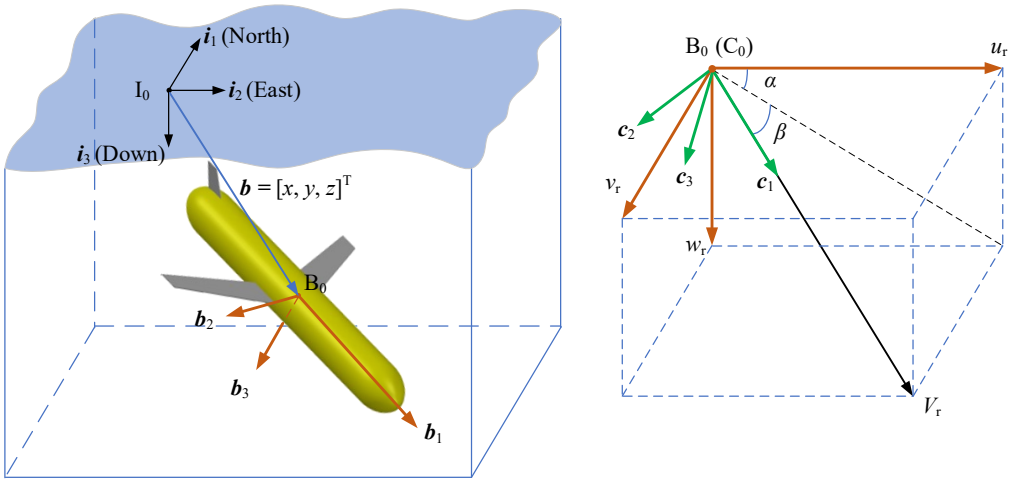

Fig. 2. The coordinate frames of an underwater glider.

Let vectors $\boldsymbol{b} = [x, y, z]^T$ and $\boldsymbol{\Psi} = [\varphi, \theta, \psi]^T$ denote the position (m) and attitude (deg) of the glider from inertial frame to body frame expressed in the inertial frame, respectively. Vectors $\boldsymbol{v} = [u, v, w]^T$ and $\boldsymbol{\omega} = [p, q, r]^T$ are defined as the translational velocity (m/s) and the rotational velocity (rad/s) of B_0

in the body frame, respectively. Since the motion of B_0 represents the motion of the whole glider, the 6 degrees of freedom (DOF) kinematic equations can be expressed as (Fossen, 2011)

$$\dot{\boldsymbol{b}} = \boldsymbol{R}_{\mathrm{B}}^{\mathrm{I}}\boldsymbol{v} \tag{1}$$

$$\dot{\boldsymbol{\Phi}} = \boldsymbol{T}_{\mathrm{B}}^{\mathrm{I}}\boldsymbol{\omega} \tag{2}$$

where $\boldsymbol{R}_{\mathrm{B}}^{\mathrm{I}}$ and $\boldsymbol{T}_{\mathrm{B}}^{\mathrm{I}}$ are the linear velocity transformation matrix and the angular velocity transformation matrix from the body frame to the inertial frame, respectively. According to (Fossen, 2011)., they can be expressed as

$$\boldsymbol{R}_{\mathrm{B}}^{\mathrm{I}} = \begin{bmatrix} \cos\theta\cos\psi & \sin\varphi\sin\theta\cos\psi - \cos\varphi\sin\psi & \cos\varphi\sin\theta\cos\psi + \sin\varphi\sin\psi \\ \cos\theta\sin\psi & \cos\varphi\cos\psi + \sin\varphi\sin\theta\sin\psi & -\sin\varphi\cos\psi + \cos\varphi\sin\theta\sin\psi \\ -\sin\theta & \sin\varphi\cos\theta & \cos\varphi\cos\theta \end{bmatrix} \tag{3}$$

$$\boldsymbol{T}_{\mathrm{B}}^{\mathrm{I}} = \begin{bmatrix} 1 & \sin\varphi\tan\theta & \cos\varphi\tan\theta \\ 0 & \cos\varphi & -\sin\varphi \\ 0 & \sin\varphi / \cos\theta & \cos\varphi / \cos\theta \end{bmatrix} \tag{4}$$

Differentiating the linear velocity transformation matrix $\boldsymbol{R}_{\mathrm{B}}^{\mathrm{I}}$ with respect to time results in (Leonard and Graver, 2001)

$$\dot{\boldsymbol{R}}_{\mathrm{B}}^{\mathrm{I}} = \boldsymbol{R}_{\mathrm{B}}^{\mathrm{I}}\boldsymbol{S}(\boldsymbol{\omega}) \tag{5}$$

For any two vectors $\boldsymbol{a} = [a_1, a_2, a_3]^{\mathrm{T}}$ and $\boldsymbol{b} = [b_1, b_2, b_3]^{\mathrm{T}}$, the rule of cross-product operator ^ is

$$\boldsymbol{S}(\boldsymbol{a})\boldsymbol{b} = \boldsymbol{a} \times \boldsymbol{b} = \begin{bmatrix} 0 & -a_3 & a_2 \\ a_3 & 0 & -a_1 \\ -a_2 & a_1 & 0 \end{bmatrix} \begin{bmatrix} b_1 \\ b_2 \\ b_3 \end{bmatrix}$$

2.2 Ocean current modelling and its impact on gliders

Here we consider a steady, but nonuniform current field, which can be defined in the inertial frame as

$$\boldsymbol{V}_{\mathrm{f}} = \left[V_{\mathrm{f1}}(\boldsymbol{b}), V_{\mathrm{f2}}(\boldsymbol{b}), V_{\mathrm{f3}}(\boldsymbol{b})\right]^{\mathrm{T}} \tag{6}$$

where $V_{\mathrm{f1}}(\boldsymbol{b})$, $V_{\mathrm{f2}}(\boldsymbol{b})$ and $V_{\mathrm{f3}}(\boldsymbol{b})$ are current velocity components along $\boldsymbol{i}_1$, $\boldsymbol{i}_2$ and $\boldsymbol{i}_3$ (m/s).

Differentiating the current velocity with respect to the position vector of the glider, we have (Wu et al., 2021b)

$$\boldsymbol{\Phi} = \frac{\mathrm{d}\boldsymbol{V}_{\mathrm{f}}}{\mathrm{d}\boldsymbol{b}^{\mathrm{T}}} = \begin{bmatrix} \dfrac{\partial V_{\mathrm{f1}}}{\partial x} & \dfrac{\partial V_{\mathrm{f1}}}{\partial y} & \dfrac{\partial V_{\mathrm{f1}}}{\partial z} \\ \dfrac{\partial V_{\mathrm{f2}}}{\partial x} & \dfrac{\partial V_{\mathrm{f2}}}{\partial y} & \dfrac{\partial V_{\mathrm{f2}}}{\partial z} \\ \dfrac{\partial V_{\mathrm{f3}}}{\partial x} & \dfrac{\partial V_{\mathrm{f3}}}{\partial y} & \dfrac{\partial V_{\mathrm{f3}}}{\partial z} \end{bmatrix} \tag{7}$$

where (Wu et al., 2021b) is the current gradient matrix. According to (Thomasson, 2000; Woolsey, 2011), we can then obtain the equivalent angular velocity of current $\boldsymbol{\Omega}_{\mathrm{f}}$ by the following equation:

$$\boldsymbol{\Omega}_{\mathrm{f}} = \boldsymbol{\Phi} - \boldsymbol{\Phi}^{\mathrm{T}} \tag{8}$$

Let $\boldsymbol{v}_{\mathrm{r}}$ and $\boldsymbol{\omega}_{\mathrm{r}}$ denote the linear velocity and angular velocity of the glider relative to the current in the body frame, respectively, and $\boldsymbol{v}_{\mathrm{f}}$ and $\boldsymbol{\omega}_{\mathrm{f}}$ denote the linear velocity and angular velocity of the current in the body frame, respectively. Then,

$$\boldsymbol{v}_{\mathrm{r}} = \boldsymbol{v} - \boldsymbol{v}_{\mathrm{f}} = \boldsymbol{v} - \boldsymbol{R}_{\mathrm{I}}^{\mathrm{B}} \boldsymbol{V}_{\mathrm{f}} = \left[u_{\mathrm{r}}, v_{\mathrm{r}}, w_{\mathrm{r}}\right]^{\mathrm{T}} \tag{9}$$

$$\boldsymbol{\omega}_{\mathrm{r}} = \boldsymbol{\omega} - \boldsymbol{\omega}_{\mathrm{f}} = \boldsymbol{\omega} - \boldsymbol{R}_{\mathrm{I}}^{\mathrm{B}} \boldsymbol{\Omega}_{\mathrm{f}} = \left[p_{\mathrm{r}}, q_{\mathrm{r}}, r_{\mathrm{r}}\right]^{\mathrm{T}} \tag{10}$$

2.3 Mass system and representation of individual parts

As shown in Fig. 3, the underwater glider can be divided into three parts. The pressure hull, the fixed wings, the ballast weights, and other objects that remain stationary in the body are regarded as the rigid body mass, denoted as m_{s}. The internal moving block, which can be moved or rotated along the $\boldsymbol{b}_1$ axis to adjust the attitude of the glider is another rigid body with mass m_{p}. Typically, the internal moving block is the battery pack of the glider. The variable ballast point mass m_{b} represents the driving mass of the glider, which is generally adjusted by changing the volume of an external bladder in the hydraulic buoyancy engine. The $\boldsymbol{l}_{\mathrm{s}} = [l_{\mathrm{s1}}, l_{\mathrm{s2}}, l_{\mathrm{s3}}]^{\mathrm{T}}$, $\boldsymbol{l}_{\mathrm{p}} = [l_{\mathrm{p1}}, l_{\mathrm{p2}}, l_{\mathrm{p3}}]^{\mathrm{T}}$ and $\boldsymbol{l}_{\mathrm{b}} = [l_{\mathrm{b1}}, l_{\mathrm{b2}}, l_{\mathrm{b3}}]^{\mathrm{T}}$ represent the vectors from I_0 to the centres of mass m_{s}, m_{p} and m_{b}, respectively. The $\boldsymbol{r}_{\mathrm{s}} = [r_{\mathrm{s1}}, r_{\mathrm{s2}}, r_{\mathrm{s3}}]^{\mathrm{T}}$, $\boldsymbol{r}_{\mathrm{p}} = [r_{\mathrm{p1}}, r_{\mathrm{p2}}, r_{\mathrm{p3}}]^{\mathrm{T}}$ and $\boldsymbol{r}_{\mathrm{b}} = [r_{\mathrm{b1}}, r_{\mathrm{b2}}, r_{\mathrm{b3}}]^{\mathrm{T}}$ represent the vectors from B_0 to the centres of mass m_{s}, m_{p} and m_{b}.

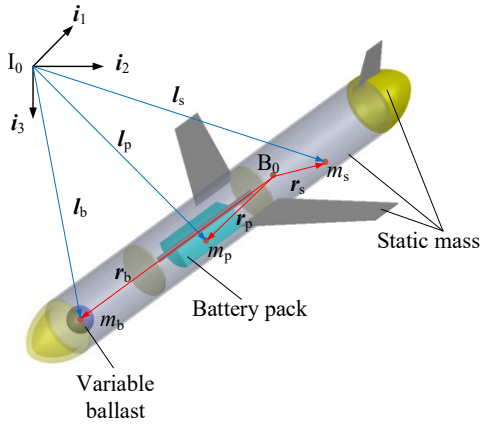

Fig. 3. The mass distribution of an underwater glide.

As shown in Fig. 4, let ζ and R_{p} denote the rotation angle and eccentric offset of the battery pack, respectively. Then the position of m_{p} in the body frame can be expressed as

$$\boldsymbol{r}_{\mathrm{p}} = [r_{\mathrm{p1}}, -R_{\mathrm{p}} \sin\zeta, R_{\mathrm{p}} \cos\zeta]^{\mathrm{T}} \tag{11}$$

where r_{p1} is the position of m_{p} along the $\boldsymbol{b}_1$ axis.

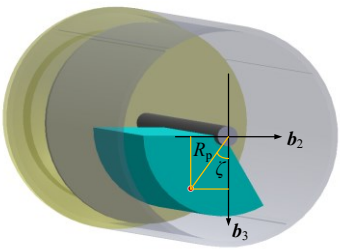

Fig. 4. The rotation of the battery pack.

Since m_b is much smaller than the total mass of the glider, and the moving distance of m_b is usually negligible, we assume that the centre of m_b is on the $\boldsymbol{b}_1$ axis, and the position is fixed. Then,

$$\boldsymbol{r}_b = [r_{b1}, 0, 0]^T \tag{12}$$

Based on the above, the linear velocity and angular velocity of the static mass in the body frame can be expressed as

$$\begin{cases} \boldsymbol{v}_s = \boldsymbol{v} + \boldsymbol{\omega} \times \boldsymbol{r}_s \\ \boldsymbol{\omega}_s = \boldsymbol{\omega} \end{cases} \tag{13}$$

The linear velocity and angular velocity of the battery pack in the body frame can be expressed as

$$\begin{cases} \boldsymbol{v}_p = \boldsymbol{v} + \boldsymbol{\omega} \times \boldsymbol{r}_p + \dot{\boldsymbol{r}}_p \\ \boldsymbol{\omega}_p = \boldsymbol{\omega} + \dot{\zeta}\, \boldsymbol{b}_1 \end{cases} \tag{14}$$

The linear velocity and angular velocity of the various ballast in the body frame can be expressed as

$$\begin{cases} \boldsymbol{v}_b = \boldsymbol{v} + \boldsymbol{\omega} \times \boldsymbol{r}_b \\ \boldsymbol{\omega}_b = \boldsymbol{\omega} \end{cases} \tag{15}$$

2.4 Forces and moments acting on the underwater glider

External forces acting on the glider include net buoyancy and hydrodynamic forces. External moments acting on the glider include moments generated by the vehicle mass system and hydrodynamic moments.

Net buoyancy is the difference between the gravity and buoyancy of the glider. Due to the seawater density gradient and the compressibility of the pressure hull, the net buoyancy of a glider will vary with the diving depth with a fixed driven mass m_b. In the inertial frame, the net buoyancy of a glider at a determined depth of z can be calculated by

$$\Delta m(z)\mathrm{g} = \left(m_b + m_s + m_p - \rho(z)\left(\frac{m_s + m_p}{p_5} - K_{vh} z \right) \right)\mathrm{g} \tag{16}$$

where $\Delta m(z)$ and K_{vh} are the net mass (kg) at depth z, the compressibility of the pressure hull of the glider, respectively, $\mathrm{g} = 9.8\ \mathrm{m/s^2}$ is the gravitational acceleration, and $\rho(z)$ is the density of the seawater ($\mathrm{kg/m^3}$) at depth z, which can be fitted by a quartic polynomial function as following (Yang et al., 2017)

$$\rho(z) = p_1 z^4 + p_2 z^3 + p_3 z^2 + p_4 z + p_5 \tag{17}$$

Then, the net buoyancy in the body frame can be expressed as

$$\boldsymbol{F}_b = \Delta m \mathrm{g} \boldsymbol{R}_I^B \boldsymbol{i}_3 \tag{18}$$

Let $\boldsymbol{T}_s$, $\boldsymbol{T}_p$ and $\boldsymbol{T}_b$ denote the moments imposed by the static mass, the battery pack and the variable ballast in the body frame, respectively. We have

$$\begin{cases} \boldsymbol{T}_s = m_s \mathrm{g}\, \boldsymbol{r}_s \times \left(\boldsymbol{R}_I^B \boldsymbol{i}_3 \right) \\ \boldsymbol{T}_p = m_p \mathrm{g}\, \boldsymbol{r}_p \times \left(\boldsymbol{R}_I^B \boldsymbol{i}_3 \right) \\ \boldsymbol{T}_b = m_b \mathrm{g}\, \boldsymbol{r}_b \times \left(\boldsymbol{R}_I^B \boldsymbol{i}_3 \right) \end{cases} \tag{19}$$

Let $\boldsymbol{F}_{\mathrm{h}}$ and $\boldsymbol{T}_{\mathrm{h}}$ denote the hydrodynamic force and moments in the body frame, respectively. Then, they can be expressed as

$$\begin{cases} \boldsymbol{F}_{\mathrm{h}} = \boldsymbol{R}_{\mathrm{V}}^{\mathrm{B}} \boldsymbol{F}_{\mathrm{h}}^{\mathrm{V}} = \boldsymbol{R}_{\mathrm{V}}^{\mathrm{B}} \begin{bmatrix} -D \\ SF \\ -L \end{bmatrix} = \boldsymbol{R}_{\mathrm{V}}^{\mathrm{B}} V_{\mathrm{r}}^2 \begin{bmatrix} -K_{\mathrm{D0}} - K_{\mathrm{D}} \alpha^2 \\ K_{\beta} \beta \\ -K_{\mathrm{L0}} - K_{\mathrm{L}} \alpha \end{bmatrix} \\ \boldsymbol{T}_{\mathrm{h}} = \boldsymbol{R}_{\mathrm{V}}^{\mathrm{B}} \boldsymbol{T}_{\mathrm{h}}^{\mathrm{V}} = \boldsymbol{R}_{\mathrm{V}}^{\mathrm{B}} \begin{bmatrix} T_{\mathrm{DL1}} \\ T_{\mathrm{DL2}} \\ T_{\mathrm{DL3}} \end{bmatrix} = \boldsymbol{R}_{\mathrm{V}}^{\mathrm{B}} V_{\mathrm{r}}^2 \begin{bmatrix} K_{\mathrm{MR}} \beta + K_{\mathrm{p}} p_{\mathrm{r}} \\ K_{\mathrm{M0}} + K_{\mathrm{M}} \alpha + K_{\mathrm{q}} q_{\mathrm{r}} \\ K_{\mathrm{MY}} \beta + K_{\mathrm{r}} r_{\mathrm{r}} \end{bmatrix} \end{cases} \tag{20}$$

where $\boldsymbol{F}_{\mathrm{h}}^{\mathrm{V}}$ and $\boldsymbol{T}_{\mathrm{h}}^{\mathrm{V}}$ are hydrodynamic forces and moments in the flow frame, respectively, D, SF and L are the hydrodynamic forces, $T_{\mathrm{DL}*}$ is the hydrodynamic moment, and K_{*} and K_{**} are coefficients of hydrodynamic forces and moments. $\boldsymbol{R}_{\mathrm{V}}^{\mathrm{B}}$ is the transformation matrix from the flow frame to the body frame, which can be expressed as

$$\boldsymbol{R}_{\mathrm{V}}^{\mathrm{B}} = \begin{bmatrix} \cos\alpha\cos\beta & -\cos\alpha\sin\beta & -\sin\alpha \\ \sin\beta & \cos\beta & 0 \\ \sin\alpha\cos\beta & -\sin\alpha\sin\beta & \cos\alpha \end{bmatrix} \tag{21}$$

The value of velocity relative to the current V_{r}, angle of attack α and a sideslip angle β can be calculated as follows:

$$V_{\mathrm{r}} = \sqrt{u_{\mathrm{r}}^2 + v_{\mathrm{r}}^2 + w_{\mathrm{r}}^2} \tag{22}$$

$$\alpha = \tan^{-1}\left(\frac{w_{\mathrm{r}}}{u_{\mathrm{r}}}\right) \tag{23}$$

$$\beta = \sin^{-1}\left(\frac{v_{\mathrm{r}}}{V_{\mathrm{r}}}\right) \tag{24}$$

Let $\boldsymbol{F}_{\mathrm{m}}$ and $\boldsymbol{T}_{\mathrm{m}}$ denote the hydrodynamic mass force and moments in the body frame, respectively. Then,

$$\begin{bmatrix} \boldsymbol{F}_{\mathrm{m}} \\ \boldsymbol{T}_{\mathrm{m}} \end{bmatrix} = -\boldsymbol{M}_{\mathrm{f}} \begin{bmatrix} \dot{\boldsymbol{v}}_{\mathrm{r}} \\ \dot{\boldsymbol{\omega}}_{\mathrm{r}} \end{bmatrix} \tag{25}$$

where $\boldsymbol{M}_{\mathrm{f}}$ is the generalized added inertia matrix. Considering a glider with two symmetry planes $\boldsymbol{b}_1\mathrm{B}_0\boldsymbol{b}_2$ and $\boldsymbol{b}_1\mathrm{B}_0\boldsymbol{b}_3$, $\boldsymbol{M}_{\mathrm{f}}$ can be written as (Yang et al., 2017)

$$\boldsymbol{M}_{\mathrm{f}} = \begin{bmatrix} \boldsymbol{M}_{\mathrm{A}} & \boldsymbol{C}_{\mathrm{A}} \\ \boldsymbol{C}_{\mathrm{A}}^{\mathrm{T}} & \boldsymbol{J}_{\mathrm{A}} \end{bmatrix} = \begin{bmatrix} \lambda_{11} & 0 & 0 & 0 & 0 & 0 \\ 0 & \lambda_{22} & 0 & 0 & 0 & \lambda_{26} \\ 0 & 0 & \lambda_{33} & 0 & \lambda_{35} & 0 \\ 0 & 0 & 0 & \lambda_{44} & 0 & 0 \\ 0 & 0 & \lambda_{53} & 0 & \lambda_{55} & 0 \\ 0 & \lambda_{62} & 0 & 0 & 0 & \lambda_{66} \end{bmatrix}$$

where $\boldsymbol{M}_{\mathrm{A}}$, $\boldsymbol{J}_{\mathrm{A}}$ and $\boldsymbol{C}_{\mathrm{A}}$ are added mass, added inertia matrix and cross term, respectively, and λ_{ij} represents the hydrodynamic inertia coefficient.

Finally, we represent these forces and moments in the form of a matrix as

$$\begin{bmatrix} \boldsymbol{F}_{\text{ext}} \\ \boldsymbol{T}_{\text{ext}} \end{bmatrix} = \begin{bmatrix} \Delta m \mathrm{g} \boldsymbol{R}_{\mathrm{I}}^{\mathrm{B}} \boldsymbol{i}_3 \\ \left(m_{\mathrm{s}} \boldsymbol{r}_s + m_{\mathrm{p}} \boldsymbol{r}_{\mathrm{p}} + m_{\mathrm{b}} \boldsymbol{r}_{\mathrm{b}} \right) \mathrm{g} \times \boldsymbol{R}_{\mathrm{I}}^{\mathrm{B}} \boldsymbol{i}_3 \end{bmatrix} + \begin{bmatrix} \boldsymbol{F}_{\mathrm{h}} \\ \boldsymbol{T}_{\mathrm{h}} \end{bmatrix} + \begin{bmatrix} \boldsymbol{F}_{\mathrm{m}} \\ \boldsymbol{T}_{\mathrm{m}} \end{bmatrix} \tag{26}$$

where $\boldsymbol{F}_{\text{ext}}$ and $\boldsymbol{T}_{\text{ext}}$ are the total force and moment expressed in the body frame.

2.5 Dynamics equations in N-E method

The dynamics equations are derived by Newton-Euler (N-E) method, which has been presented in many literatures (Leonard and Graver, 2001; Wu et al., 2021b). Since dynamic modeling is not the main focus of this study, only the final results, presented in Eq. (27), are provided here. The detailed modelling process can be found in Appendix A.

$$\begin{aligned} &\begin{bmatrix} m_{\mathrm{s}} \boldsymbol{I} + m_{\mathrm{p}} \boldsymbol{I} & -m_{\mathrm{s}} \$_{\mathrm{s}} - m_{\mathrm{p}} \$_{\mathrm{p}} \\ m_{\mathrm{s}} \$_{\mathrm{s}} + m_{\mathrm{p}} \$_{\mathrm{p}} & \left(\boldsymbol{J}_{\mathrm{s}} + \boldsymbol{J}_{\mathrm{p}} \right) - m_{\mathrm{p}} \$_{\mathrm{p}} \$_{\mathrm{p}} \end{bmatrix} \begin{bmatrix} \dot{\boldsymbol{v}} \\ \dot{\boldsymbol{\omega}} \end{bmatrix} \\ &= m_{\mathrm{s}} \begin{bmatrix} \boldsymbol{v}_{\mathrm{s}} \times \boldsymbol{\omega} \\ \boldsymbol{r}_{\mathrm{s}} \times \boldsymbol{v} \times \boldsymbol{\omega} + \boldsymbol{\omega} \times \boldsymbol{r}_{\mathrm{s}} \times \boldsymbol{v} \end{bmatrix} + \begin{bmatrix} \boldsymbol{0} \\ \left(\boldsymbol{J}_{\mathrm{s}} \boldsymbol{\omega} \right) \times \boldsymbol{\omega} \end{bmatrix} + m_{\mathrm{p}} \begin{bmatrix} \boldsymbol{v}_{\mathrm{p}} \times \boldsymbol{\omega} + \dot{\boldsymbol{r}}_{\mathrm{p}} \times \boldsymbol{\omega} \\ \boldsymbol{r}_{\mathrm{p}} \times \left(\boldsymbol{v}_{\mathrm{p}} \times \boldsymbol{\omega} + \dot{\boldsymbol{r}}_{\mathrm{p}} \times \boldsymbol{\omega} \right) \end{bmatrix} \\ &- \begin{bmatrix} m_{\mathrm{p}} \ddot{\boldsymbol{r}}_{\mathrm{p}} \\ \boldsymbol{J}_{\mathrm{p}} \dot{\zeta} \boldsymbol{b}_{\mathrm{l}} + m_{\mathrm{p}} \boldsymbol{r}_{\mathrm{p}} \times \ddot{\boldsymbol{r}}_{\mathrm{p}} \end{bmatrix} + \begin{bmatrix} \boldsymbol{0} \\ \left(\boldsymbol{J}_{\mathrm{p}} \boldsymbol{\omega}_{\mathrm{p}} \right) \times \boldsymbol{\omega}_{\mathrm{p}} \end{bmatrix} + \begin{bmatrix} \boldsymbol{0} \\ \boldsymbol{J}_{\mathrm{p}} \left(\dot{\zeta} \boldsymbol{b}_{\mathrm{l}} \times \boldsymbol{\omega} \right) \end{bmatrix} + \begin{bmatrix} \boldsymbol{F}_{\text{ext}} \\ \boldsymbol{T}_{\text{ext}} \end{bmatrix} \end{aligned} \tag{27}$$

where $\boldsymbol{I}$ is a 3×3 identity matrix, $\boldsymbol{J}_{\mathrm{s}}$ is the inertia matrixes of the m_{s}, $\boldsymbol{J}_{\mathrm{p}}$ is the inertial matrix of the battery pack which can be expressed as

$$\begin{cases} \boldsymbol{J}_{\mathrm{p}} = \boldsymbol{R}_{\mathrm{p}}^{\mathrm{b}} \boldsymbol{J}_{\mathrm{p}}^{0} \left(\boldsymbol{R}_{\mathrm{p}}^{\mathrm{b}} \right)^{\mathrm{T}} \\ \boldsymbol{R}_{\mathrm{p}}^{\mathrm{b}} = \begin{bmatrix} 1 & 0 & 0 \\ 0 & \cos\zeta & -\sin\zeta \\ 0 & \sin\zeta & \cos\zeta \end{bmatrix} \end{cases} \tag{28}$$

where $\boldsymbol{J}_{\mathrm{p}}^{0}$ is the initial inertial matrix when the battery pack is in the stationary state with $\zeta = 0$.

To validate the dynamics model, a dedicated research effort was undertaken, as demonstrated in our previous study (Wu et al., 2022).

3 Controller design and numerical modelling

Underwater gliders glide primarily move in a sawtooth-like motion to translate from point A to B. The objective of the controller is to guide the underwater glider along the predetermined trajectory while maintaining the desired gliding velocity, pitch and heading angle to allow gliders to perform the required missions.

In this Section, the feedforward and feedback controller is designed and modelled. The feedforward control generates initial control inputs based on the estimation of the equilibrium dynamics model under steady conditions. Subsequently, the feedback control fine-tunes the control parameters to minimise deviations from the target setpoints. In this study, LQR is designed for feedback control in the vertical and horizontal planes, respectively. Since LQR is a linear controller, we first linearize the dynamics equations.

3.1 Linearization of the dynamics equations

3.1.1 Linearization in the vertical plane

When an underwater glider moves along a sawtooth-like trajectory in the vertical plane, its motion involves movement along the $\boldsymbol{b}_1$ and $\boldsymbol{b}_3$ axes, as well as rotation along $\boldsymbol{b}_2$ axis. Therefore, we have

$$\boldsymbol{\Theta} = [0,\ \theta,\ 0]^{\mathrm{T}}$$
$$\boldsymbol{v} = [u,\ 0,\ w]^{\mathrm{T}}$$
$$\boldsymbol{\omega} = [0,\ q,\ 0]^{\mathrm{T}}$$
$$\zeta = 0$$

Since the position static mass m_{s} is generally on the $\boldsymbol{b}_1\mathrm{B}_0\boldsymbol{b}_3$ plane, we can set $r_{\mathrm{s}2}$ to 0. In addition, we consider that the moving velocity of the battery pack $\dot{r}_{\mathrm{p}1}$ is constant, which consequently results in $\ddot{r}_{\mathrm{p}1} = 0$. Substituting these above into Eqs. (2) and (27), we have the following dynamics equations in the vertical plane (these equations are obtained by Maple 2021.0).

$$\dot{u} = \frac{1}{\left(m_{\mathrm{s}} + m_{\mathrm{p}} + \lambda_{11}\right)}\left(\left(-m_{\mathrm{s}} - m_{\mathrm{p}}\right)wq + \left(m_{\mathrm{s}}r_{\mathrm{s}1} + m_{\mathrm{p}}r_{\mathrm{p}1}\right)q^2 - \left(m_{\mathrm{p}}R_{\mathrm{p}} + m_{\mathrm{s}}r_{\mathrm{s}3}\right)\dot{q} + F_1\right) \tag{29}$$

$$\dot{w} = \frac{1}{\left(m_{\mathrm{s}} + m_{\mathrm{p}} + \lambda_{33}\right)}\left(\left(m_{\mathrm{s}} + m_{\mathrm{p}}\right)uq + \left(m_{\mathrm{s}}r_{\mathrm{s}3} + m_{\mathrm{p}}R_{\mathrm{p}}\right)q^2 + 2m_{\mathrm{p}}\dot{r}_{\mathrm{p}1}q + \left(m_{\mathrm{p}}r_{\mathrm{p}1} + m_{\mathrm{s}}r_{\mathrm{s}1} - \lambda_{35}\right)\dot{q} + F_3\right) \tag{30}$$

$$\dot{q} = \frac{1}{\left(J_{\mathrm{s}22} + J_{\mathrm{p}22}^0 + m_{\mathrm{p}}R_{\mathrm{p}}{}^2 + m_{\mathrm{p}}r_{\mathrm{p}1}{}^2 + \lambda_{55}\right)}\begin{pmatrix}\left(-m_{\mathrm{p}}r_{\mathrm{p}1} - m_{\mathrm{s}}r_{\mathrm{s}1}\right)uq + \left(-m_{\mathrm{p}}R_{\mathrm{p}} - m_{\mathrm{s}}r_{\mathrm{s}3}\right)wq \\ -2m_{\mathrm{p}}r_{\mathrm{p}1}\dot{r}_{\mathrm{p}1}q - \left(m_{\mathrm{s}}r_{\mathrm{s}3} + m_{\mathrm{p}}R_{\mathrm{p}}\right)\dot{u} \\ +\left(m_{\mathrm{p}}r_{\mathrm{p}1} + m_{\mathrm{s}}r_{\mathrm{s}1} - \lambda_{53}\right)\dot{w} + T_2\end{pmatrix} \tag{31}$$

$$\dot{\theta} = q \tag{32}$$

where

$$F_1 = -m_{\mathrm{b}}\mathrm{g}\sin\theta - D\cos\alpha + L\sin\alpha$$

$$F_3 = m_{\mathrm{b}}\mathrm{g}\cos\theta - D\sin\alpha - L\cos\alpha$$

$$T_2 = m_{\mathrm{s}}\mathrm{g}\left(-r_{\mathrm{s}1}\cos\theta - r_{\mathrm{s}3}\sin\theta\right) + m_{\mathrm{p}}\mathrm{g}\left(-r_{\mathrm{p}1}\cos\theta - R_{\mathrm{p}}\sin\theta\right) - m_{\mathrm{b}}\mathrm{g}r_{\mathrm{b}1}\cos\theta + T_{\mathrm{DL}2}$$

Here, we consider a particular state of equilibrium in which the position of the battery pack remains stationary relative to the glider body. Additionally, the glider operates with a constant pitch angle during descent or ascent. In this case, we have $\dot{r}_{\mathrm{p}1} = 0$, $\dot{\theta} = q = 0$, $\dot{u} = 0$, and $\dot{w} = 0$. Substituting these into Eqs. (29) ~ (32) gives the dynamics equations at the desired glide equilibria:

$$0 = -m_{\mathrm{bd}}\mathrm{g}\sin\theta_{\mathrm{d}} - D_{\mathrm{d}}\cos\alpha_{\mathrm{d}} + L_{\mathrm{d}}\sin\alpha_{\mathrm{d}} \tag{33}$$

$$0 = m_{\mathrm{bd}}\mathrm{g}\cos\theta_{\mathrm{d}} - D_{\mathrm{d}}\sin\alpha_{\mathrm{d}} - L_{\mathrm{d}}\cos\alpha_{\mathrm{d}} \tag{34}$$

$$0 = m_{\mathrm{s}}\mathrm{g}\left(-r_{\mathrm{s}1}\cos\theta_{\mathrm{d}} - r_{\mathrm{s}3}\sin\theta_{\mathrm{d}}\right) + m_{\mathrm{p}}\mathrm{g}\left(-r_{\mathrm{p}1\mathrm{d}}\cos\theta_{\mathrm{d}} - R_{\mathrm{p}}\sin\theta_{\mathrm{d}}\right) - m_{\mathrm{bd}}\mathrm{g}r_{\mathrm{b}1}\cos\theta_{\mathrm{d}} + T_{\mathrm{DL}2\mathrm{d}} \tag{35}$$

where subscript ‘d’ represents the value at the desired equilibrium point.

As shown in Fig. 5, let γ_d denote the desired gliding angle which represents the angle between the $\boldsymbol{i}_1\mathrm{I}_0\boldsymbol{i}_2$ plane and the velocity of the glider. Then,

$$\gamma_d = \theta_d - \alpha_d \tag{36}$$

Rewriting Eqs. (33) and (34) in matrix form results in (Leonard and Graver, 2001)

$$\begin{aligned}\begin{bmatrix} 0 \\ m_{bd}g \end{bmatrix} &= \begin{bmatrix} \cos\theta_d & \sin\theta_d \\ -\sin\theta_d & \cos\theta_d \end{bmatrix}\begin{bmatrix} \cos\alpha_d & -\sin\alpha_d \\ \sin\alpha_d & \cos\alpha_d \end{bmatrix}\begin{bmatrix} L_d \\ D_d \end{bmatrix} \\ &= \begin{bmatrix} \cos\gamma_d & \sin\gamma_d \\ -\sin\gamma_d & \cos\gamma_d \end{bmatrix}\begin{bmatrix} K_{D0} + K_D{\alpha_d}^2 \\ K_{L0} + K_L\alpha_d \end{bmatrix}{V_d}^2\end{aligned} \tag{37}$$

According to the first line of Eq. (37), if the desired gliding velocity is $V_d \neq 0$ and we have desired gliding angle γ_d ($\gamma_d \neq 0$), the corresponding angle of attack can be calculated by

$$\alpha_d = \frac{1}{2}\frac{K_L}{K_D}\tan\gamma_d\left(-1+\sqrt{1-4\frac{K_D}{K_L^2}\cot\gamma_d\left(K_{D0}\cot\gamma_d + K_{L0}\right)}\right) \tag{38}$$

With the desired gliding velocity V_d, the desired translational velocity in the body frame can be expressed as

$$u_d = V_d\cos\alpha_d \tag{39}$$

$$w_d = V_d\sin\alpha_d \tag{40}$$

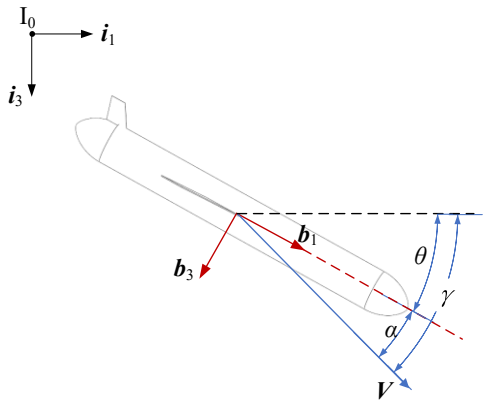

Fig. 5. Gliding angle.

According to the second line of Eq. (37), the desired mass of variable ballast at the equilibrium point can be calculated by

$$m_{bd} = \frac{V_d^2}{g}\left(-\left(K_{D0} + K_D{\alpha_d}^2\right)\sin\gamma_d + \left(K_{L0} + K_L\alpha_d\right)\cos\gamma_d\right) \tag{41}$$

Then, the desired position of the battery pack along the $\boldsymbol{b}_1$ axis can be calculated by Eq. (35) as follow

$$r_{p1d} = \frac{m_s g\left(-r_{s1}\cos\theta_d - r_{s3}\sin\theta_d\right) - m_{bd}gr_{b1}\cos\theta_d + T_{DL2d}}{m_p g\cos\theta_d} - R_p\tan\theta_d \tag{42}$$

With the motion parameters at the desired equilibrium point, the dynamics equations can be then linearized around the point. Define the state variable and control input as $\boldsymbol{x} = [u, w, q, \theta]^{\mathrm{T}}$ and $\boldsymbol{u} = [r_{\mathrm{p1}}, m_{\mathrm{b}}]^{\mathrm{T}}$, respectively. At the desired equilibrium point, $\boldsymbol{x}_{\mathrm{d}} = [u_{\mathrm{d}}, w_{\mathrm{d}}, q_{\mathrm{d}}, \theta_{\mathrm{d}}]^{\mathrm{T}}$ and $\boldsymbol{u}_{\mathrm{d}} = [r_{\mathrm{p1d}}, m_{\mathrm{bd}}]^{\mathrm{T}}$. Considering small disturbances $\Delta\boldsymbol{x} = [\Delta u, \Delta w, \Delta q, \Delta\theta]^{\mathrm{T}}$ and $\Delta\boldsymbol{u} = [\Delta r_{\mathrm{p1}}, \Delta m_{\mathrm{b}}]^{\mathrm{T}}$, it results in

$$\begin{cases} \boldsymbol{x} = \boldsymbol{x}_{\mathrm{d}} + \Delta\boldsymbol{x} \\ \boldsymbol{u} = \boldsymbol{u}_{\mathrm{d}} + \Delta\boldsymbol{u} \end{cases}$$

Then the linearized equation is

$$\Delta\dot{\boldsymbol{x}} = \boldsymbol{A}\Delta\boldsymbol{x} + \boldsymbol{B}\Delta\boldsymbol{u}$$

where $\boldsymbol{A}$ is the state matrix and $\boldsymbol{B}$ is the input matrix. Let G_1, G_2, G_3 and G_4 denote the Eqs. (29) ~ (32), respectively. If x_l (l = 1, 2, 3, 4) and u_m (m = 1, 2) represent the l^{th} and m^{th} element of the state variable $\boldsymbol{x}$ and control input $\boldsymbol{u}$, respectively, the $\boldsymbol{A}$ and $\boldsymbol{B}$ can be expressed as

$$\boldsymbol{A} = \begin{bmatrix} \dfrac{\partial G_1}{\partial x_1} & \cdots & \dfrac{\partial G_1}{\partial x_4} \\ \vdots & \ddots & \vdots \\ \dfrac{\partial G_4}{\partial x_1} & \cdots & \dfrac{\partial G_4}{\partial x_4} \end{bmatrix}\Bigg|_{(\boldsymbol{x}_{\mathrm{d}},\ \boldsymbol{u}_{\mathrm{d}})} \text{ and } \boldsymbol{B} = \begin{bmatrix} \dfrac{\partial G_1}{\partial u_1} & \dfrac{\partial G_1}{\partial u_2} \\ \vdots & \vdots \\ \dfrac{\partial G_4}{\partial u_1} & \dfrac{\partial G_4}{\partial u_2} \end{bmatrix}\Bigg|_{(\boldsymbol{x}_{\mathrm{d}},\ \boldsymbol{u}_{\mathrm{d}})}$$

For convenience, we omit $\cdot|(\boldsymbol{x}_{\mathrm{d}}, \boldsymbol{u}_{\mathrm{d}})$ from the expression of the partial derivative. Recalling that $q_{\mathrm{d}} = 0$ and $\dot{r}_{\mathrm{p1d}} = 0$ at an equilibrium point, the elements in $\boldsymbol{A}$ and $\boldsymbol{B}$ can be expressed as in Appendix B.

3.1.2 Linearization in the horizontal plane

When an underwater glider moves in the horizontal plane, its motion involves the movement along the $\boldsymbol{b}_2$ axis and the rotation around the $\boldsymbol{b}_1$ and $\boldsymbol{b}_3$ axes. Due to the coupling between the motions in the vertical and horizontal planes, we take the remaining equations in the Eqs. (2) and (27) except for in the vertical plane and keep the state variable and control input in the vertical plane. In addition, we consider that the angular velocity of the battery pack $\dot{\zeta}$ is constant. Then,

$$\begin{aligned} &\left(m_{\mathrm{s}} + m_{\mathrm{p}}\right)\dot{v} \\ &= m_{\mathrm{s}}\left(-\left(u + qr_{\mathrm{s3}}\right)r + \left(w - qr_{\mathrm{s1}}\right)p\right) \\ &+ m_{\mathrm{p}}\begin{pmatrix} -\left(u + qR_{\mathrm{p}}\cos\zeta + rR_{\mathrm{p}}\sin\zeta + \dot{r}_{\mathrm{p1}}\right)r \\ +\left(w - pR_{\mathrm{p}}\sin\zeta - qr_{\mathrm{p1}} - R_{\mathrm{p}}\dot{\zeta}\sin\zeta\right)p \\ -\dot{r}_{\mathrm{p1}}r - R_{\mathrm{p}}\dot{\zeta}\sin\zeta p \end{pmatrix} \\ &- m_{\mathrm{p}}R_{\mathrm{p}}\dot{\zeta}\sin\zeta + \left(m_{\mathrm{p}}R_{\mathrm{p}}\cos\zeta + m_{\mathrm{s}}r_{\mathrm{s3}}\right)\dot{p} - \left(m_{\mathrm{p}}r_{\mathrm{p1}} + m_{\mathrm{s}}r_{\mathrm{s1}}\right)\dot{r} + F_2 \end{aligned} \tag{43}$$

$$
\begin{aligned}
&\left(J_{s11}+J_{p11}^{0}+m_{p}R_{p}^{2}\cos^{2}\zeta+m_{p}R_{p}^{2}\sin^{2}\zeta\right)\dot{p}\\
&=m_{s}\left(\left(-r_{s1}w+r_{s3}u\right)r+\left(-pr_{s3}+rr_{s1}\right)w\right)\\
&+J_{s22}qr-\left(J_{s31}p+J_{s33}r\right)q\\
&+m_{p}\begin{pmatrix}-R_{p}\sin\zeta\begin{pmatrix}\left(u+qR_{p}\cos\zeta+rR_{p}\sin\zeta+\dot{r}_{p1}\right)q\\-\left(v-pR_{p}\cos\zeta+rr_{p1}-R_{p}\dot{\zeta}\cos\zeta\right)p+\dot{r}_{p1}q+R_{p}\dot{\zeta}\cos\zeta p\end{pmatrix}\\-R_{p}\cos\zeta\begin{pmatrix}-\left(u+qR_{p}\cos\zeta+rR_{p}\sin\zeta+\dot{r}_{p1}\right)r\\+\left(w-pR_{p}\sin\zeta-qr_{p1}-R_{p}\dot{\zeta}\sin\zeta\right)p-\dot{r}_{p1}r-R_{p}\dot{\zeta}\sin\zeta p\end{pmatrix}\end{pmatrix}\\
&+\left(\left(\cos^{2}\zeta J_{p22}^{0}+\sin^{2}\zeta J_{p33}^{0}\right)q+\left(\cos\zeta\sin\zeta J_{p22}^{0}-\sin\zeta\cos\zeta J_{p33}^{0}\right)r\right)r\\
&-\left(\left(\cos\zeta\sin\zeta J_{p22}^{0}-\sin\zeta\cos\zeta J_{p33}^{0}\right)q+\left(\sin^{2}\zeta J_{p22}^{0}+\cos^{2}\zeta J_{p33}^{0}\right)r\right)q\\
&+\left(m_{p}R_{p}\cos\zeta+m_{s}r_{s3}\right)\dot{w}+m_{p}R_{p}\sin\zeta\dot{u}-m_{p}R_{p}\sin\zeta r_{p1}\dot{q}-\left(J_{s13}-m_{p}R_{p}\cos\zeta r_{p1}\right)\dot{q}+T_{1}
\end{aligned}
\tag{44}
$$

$$
\begin{aligned}
&\left(J_{s33}+\sin^{2}\zeta J_{p22}^{0}+\cos^{2}\zeta J_{p33}^{0}+m_{p}R_{p}^{2}\sin^{2}\zeta+m_{p}r_{p1}^{2}\right)\dot{r}\\
&=m_{s}\left(-\left(-r_{s1}w+r_{s3}u\right)p-\left(-pr_{s3}+rr_{s1}\right)u\right)+\left(J_{s11}p+J_{s13}r\right)q\\
&-J_{s22}pq\\
&+m_{p}\begin{pmatrix}r_{p1}\begin{pmatrix}\begin{pmatrix}-\left(u+qR_{p}\cos\zeta+rR_{p}\sin\zeta+\dot{r}_{p1}\right)r+\left(w-pR_{p}\sin\zeta-qr_{p1}-R_{p}\dot{\zeta}\sin\zeta\right)p\end{pmatrix}\\-\dot{r}_{p1}r-R_{p}\dot{\zeta}\sin\zeta p\end{pmatrix}\\+R_{p}\sin\zeta\begin{pmatrix}\left(v-pR_{p}\cos\zeta+rr_{p1}-R_{p}\dot{\zeta}\cos\zeta\right)r\\\left(w-pR_{p}\sin\zeta-qr_{p1}-R_{p}\dot{\zeta}\sin\zeta\right)q\\-R_{p}\dot{\zeta}\cos\zeta r+R_{p}\dot{\zeta}\sin\zeta q\end{pmatrix}\end{pmatrix}\\
&+J_{p11}^{0}\left(p+\dot{\zeta}\right)q\\
&-\left(\left(\cos^{2}\zeta J_{p22}^{0}+\sin^{2}\zeta J_{p33}^{0}\right)q+\left(\cos\zeta\sin\zeta J_{p22}^{0}-\sin\zeta\cos\zeta J_{p33}^{0}\right)r\right)\left(p+\dot{\zeta}\right)\\
&-\left(\cos\zeta\sin\zeta J_{p22}^{0}-\sin\zeta\cos\zeta J_{p33}^{0}\right)\dot{\zeta}r+\left(\sin^{2}\zeta J_{p22}^{0}+\cos^{2}\zeta J_{p33}^{0}\right)\dot{\zeta}q\\
&-m_{p}R_{p}\sin\zeta\dot{u}-\left(m_{p}r_{p1}+m_{s}r_{s1}\right)\dot{w}-\left(J_{s31}-m_{p}R_{p}\cos\zeta r_{p1}\right)\dot{p}\\
&-\left(\cos\zeta J_{p22}^{0}\sin\zeta-\sin\zeta J_{p33}^{0}\cos\zeta+m_{p}R_{p}^{2}\cos\zeta\sin\zeta\right)\dot{q}\\
&+T_{3}
\end{aligned}
\tag{45}
$$

$$\dot{\varphi}=p+q\sin\varphi\tan\theta+r\cos\varphi\tan\theta \tag{46}$$

$$\dot{\psi}=q\sin\varphi\sec\theta+r\cos\varphi\sec\theta \tag{47}$$

where

$$F_{2}=m_{b}g\sin\varphi\cos\theta-D\sin\beta+SF\cos\beta$$

$$T_{1}=-m_{s}gr_{s3}\sin\varphi\cos\theta-m_{p}gR_{p}\cos\theta\left(\sin\zeta\cos\varphi+\cos\zeta\sin\varphi\right)+T_{DL1}\cos\alpha\cos\beta-T_{DL2}\cos\alpha\sin\beta-T_{DL3}\sin\alpha$$

$$T_3 = m_s g r_{s1} \sin\varphi\cos\theta + m_p g\left(r_{p1}\sin\varphi\cos\theta - R_p \sin\zeta\sin\theta\right) + m_b g r_{b1}\sin\varphi\cos\theta + T_{DL1}\sin\alpha\cos\beta - T_{DL2}\sin\alpha\sin\beta + T_{DL3}\cos\alpha$$

The state variable and control input are defined as $\boldsymbol{x} = [v, p, r, \varphi, \psi]^T$ and $u = \zeta$. At the desired equilibrium point, $\boldsymbol{x}_d = [v_d, p_d, r_d, \varphi_d, \psi_d]^T$ and $u_d = \zeta_d$. Recalling the control objective, the glider is expected to perform as much sawtooth-like motion as possible. Therefore, during steady state operation, $v_d = 0$, $p_d = 0$, $r_d = 0$, $\varphi_d = 0$ and $\zeta_d = 0$. The horizontal dynamics equations can be then linearized using the same method in Section 3.1.1. The elements in the state matrix $\boldsymbol{A}$ and input matrix $\boldsymbol{B}$ in the horizontal plane can be expressed as in Appendix C.

3.2 Design of the motion controller

In this study, a control strategy is developed by combining the feedforward control with the LQR, which is designed based on the state matrix $\boldsymbol{A}$ and the input matrix $\boldsymbol{B}$. The LQR provides optimally controlled feedback gains by operating a dynamic system at a minimum cost, which can be described by the following cost function:

$$J = \int_0^\infty \left(\boldsymbol{x}^T \boldsymbol{Q}\boldsymbol{x} + \boldsymbol{u}^T \boldsymbol{R}\boldsymbol{u}\right) \mathrm{d}t$$

where $\boldsymbol{Q}$ and $\boldsymbol{R}$ set weights of state deviation and input usage. In this case, we can find an optimal feedback control law as

$$\boldsymbol{u}^* = -\boldsymbol{K}\boldsymbol{x}$$

where $\boldsymbol{K}$ is the feedback gain which can be calculated using the matrices $\boldsymbol{A}$, $\boldsymbol{B}$, $\boldsymbol{Q}$ and $\boldsymbol{R}$.

Figure 6 illustrates the structure of the feedforward and LQR feedback controller for the underwater glider. With the desired gliding velocity V_d, the pitch angle θ_d and the heading angle ψ_d, the desired motion state variable $\boldsymbol{x}_d$ and the control input $\boldsymbol{u}_d$ can be first obtained by solving the dynamics equations in a steady condition. Note that with the desired pitch angle θ_d, the desired gliding angle γ_d can be obtained by solving the Eqs. (36) and (38) numerically. Then, according to the error $\Delta\boldsymbol{x}$ between the measured and the desired, the LQR generates an optimal $\Delta\boldsymbol{u}$ to update the control input with $\boldsymbol{u}_d + \Delta\boldsymbol{u}$. In this study, LQR is designed separately in the vertical and horizontal planes. Let subscripts '_vtc' and '_hrz' denote the horizontal and vertical planes, individually. The feedback gain $\boldsymbol{K}$ is calculated using MATLAB.

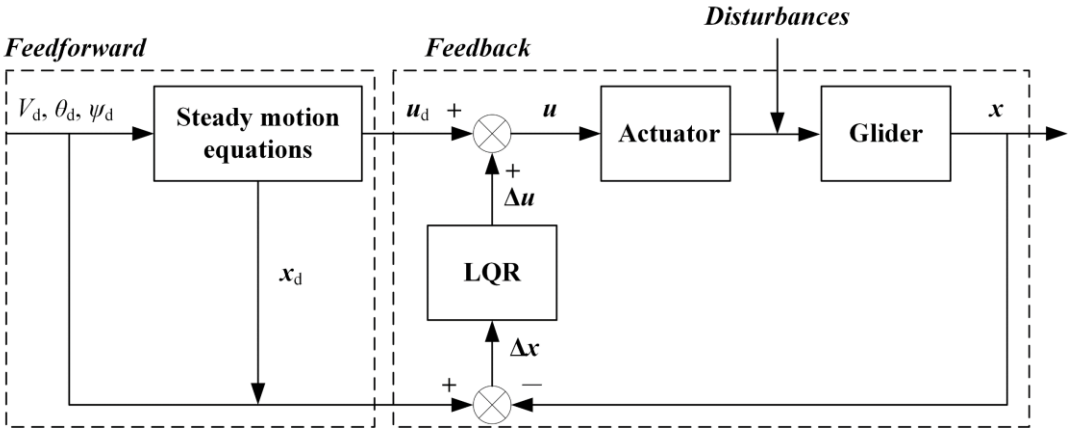

Fig. 6. Structure of feedforward and LQR feedback controller.

4 Establish the energy consumption model and propose the motion accuracy quantification method

4.1 Energy consumption model

The energy consumption model for an underwater glider is used to estimate the electric energy consumed during its operation. By considering the primary energy consumers and quantifying their energy consumption, the energy consumption model provides valuable insights into the overall energy usage of the underwater glider. This information can aid in optimizing design choices and operational strategies to achieve energy-efficient performance. The primary energy consumers of the glider are identified as follows:

(1) Buoyancy engine that controls the net mass (net buoyancy) m_{b}.
(2) Attitude regulator (battery pack and its drive system) that controls the roll, pitch, and yaw angles.
(3) Control-navigation-detection (CND) system which can acquire data, process information, and generate control commands for autonomy.
(4) The communication system that exchanges data with the shore station.

As the communication system only works when the glider is on the surface, it does not affect the energy consumption operating underwater that is focussed on in this paper. Therefore, the energy consumed by the communication system will not be included.

4.1.1 Energy consumption of the buoyancy engine

The power of the buoyancy engine varies with the operating depth z and the flow rate which leads to the change of the net mass $\dot{m}_{\mathrm{b}}$. Let E_{b} and P_{b} denote the energy consumption (J) and power (W) of the buoyancy engine in one working cycle, respectively. Then,

$$E_{\mathrm{b}}=\int_{0}^{t_{\mathrm{all}}} P_{\mathrm{b}}\left(z, \dot{m}_{\mathrm{b}}\right) \mathrm{d}t \tag{48}$$

where t_{all} is the total time (s) when the glider is operating under water.

4.1.2 Energy consumption of the attitude regulator

The power of the attitude regulator is mainly determined by the translational and angular velocities of the internal moving block and the attitude of the glider. Let E_{p} and P_{p} denote the energy consumption and power of the attitude regulator in one cycle, respectively. Then,

$$E_{\mathrm{p}}=\int_{0}^{t_{\mathrm{all}}} P_{\mathrm{p}}\left(\boldsymbol{\Psi}, \dot{r}_{\mathrm{p1}}, \dot{\zeta}\right) \mathrm{d}t \tag{49}$$

4.1.3 Energy consumption of the CND system

The power of the CND system is related to the state of the sensor, the operating frequency of the processor, etc. In this study, we use the operating time t_{all} and average power of the CND system P_{CND} to calculate its energy consumption. Let E_{CND} denote the energy consumption of the CND system. Then,

$$E_{\mathrm{CND}}=P_{\mathrm{CND}} t_{\mathrm{all}} \tag{50}$$

The energy consumption of a glider in one working cycle E can be obtained by adding up the energy consumption of each part as follows

$$E=E_{\mathrm{b}}+E_{\mathrm{p}}+E_{\mathrm{CND}}$$

Evaluation of energy consumption and motion accuracy for underwater gliders based on quadrant analysis

To investigate the energy efficiency of the glider, the energy consumption in one working cycle is nondimensionalised by diving it by the total onboard energy of the glider E_t. Let ˜ represent the dimensionless quantity. The dimensionless E can be expressed as

$$\tilde{E} = E/E_t$$

4.2 Motion accuracy evaluation

Motion accuracy represents how close the actual motion parameters match with the targets. The target motion parameters generally refer to the desired gliding velocity V_d, the pitch angle θ_d and the heading angle ψ_d. Let $S_{dn} = [V_{dn}, \theta_{dn}, \psi_{dn}]$ and $S_n = [V_n, \theta_n, \psi_n]$ denote the target and measured (or predicted) vectors of motion for times n ($n = 1, 2,\ldots, N$). Since values vary from mission to mission, the parameters are nondimensionalized by dividing the maximum velocity V_{max} ($V_{max} \neq 0$), π/2, and π, respectively. Then, we have

$$\tilde{S}_{dn} = \left[V_{dn}/V_{max},\ 2\theta_{dn}/\pi,\ \psi_{dn}/\pi\right]$$

$$\tilde{S}_n = \left[V_n/V_{max},\ 2\theta_n/\pi,\ \psi_n/\pi\right]$$

Based on this, the motion accuracy can be then evaluated by dimensionless root-mean-square error (RMSE), which can be computed by

$$\tilde{\varepsilon} = \sqrt{\frac{\sum_{n=1}^{N}\left(\tilde{S}_n - \tilde{S}_{dn}\right)^2}{N}}$$

where the smaller $\tilde{\varepsilon}$ means the higher motion accuracy.

Based on these, let $\tilde{E}_{LQR}$ and $\tilde{E}_{OL}$ denote the dimensionless energy consumption with/without LQR control, respectively, so are the $\tilde{\varepsilon}_{LQR}$ and $\tilde{\varepsilon}_{OL}$. The percentage changes in energy consumption δ_E and motion accuracy δ_ε caused by LQR can then be expressed as

$$\delta_E = \frac{\tilde{E}_{LQR} - \tilde{E}_{OL}}{\tilde{E}_{OL}} \times 100\%$$

$$\delta_\varepsilon = \frac{\tilde{\varepsilon}_{LQR} - \tilde{\varepsilon}_{OL}}{\tilde{\varepsilon}_{OL}} \times 100\%$$

Then a two-dimensional coordinate system, namely a quadrant chart with δ_ε as the horizontal axis and δ_E as the vertical axis, can be introduced to illustrate the energy consumption and the motion accuracy of the LQR. A Quadrant chart is technically a scatter plot that is divided into four quadrants, in which performance under two parameters is assessed for each entity. It has been a very common tool for decision making, especially in turbulence research (Mangan et al., 2022), medicine (Yan et al., 2021), business (Hamid et al., 2022), etc.

The physical meaning of the results in the different quadrants is explained in Fig. 7. Based on this chart, the performance of the controller can be quickly evaluated, which means that the balance between energy consumption and motion accuracy under feedback control can be quantitatively achieved. Moreover, the operational strategy corresponding to the optimal performance of the controller can be found. The method of application of the quadrant chart will be illustrated in the following case study.

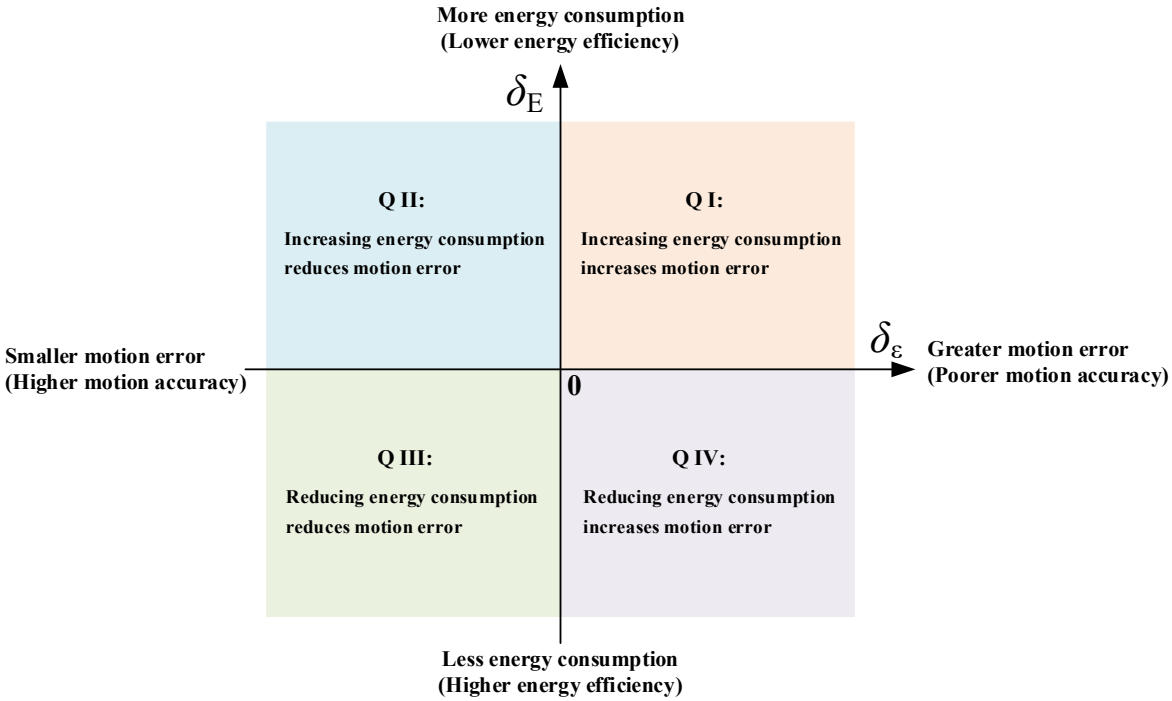

Fig. 7. Quadrant chart of energy-accuracy of underwater gilders.

5 Case study and result discussion

5.1 Specification of the study subject and basic setup

The Petrel-II glider is used as an example to investigate the effects of the LQR on energy consumption and motion accuracy. As shown in Fig. 8, the Petrel-II glider features a torpedo-shaped body with two fixed horizontal wings and a vertical surface. . It is equipped with a lithium-ion battery pack, providing a total energy of 18.9 MJ (Song et al., 2020). The main specifications of the Petrel-II glider are shown in Table 1. The mass and geometric characteristic parameters and the hydrodynamic coefficients can be found in Appendix D with the water density gradient specified for ocean conditions.

Fig. 8. Petrel-II underwater glider.

Table 1 Main specifications of the Petrel-II glider

Technical specification	Value
Diameter	0.22 m
Length (not including antenna)	2.30 m
Design depth	1,500 m
Gliding range	1,500 km

According to our previous experiments conducted on Petrel-II glider (Song et al., 2020; Wu et al., 2021b), the power of the buoyancy engine can be expressed as follows:

$$P_{\mathrm{b}}=\begin{cases}0.01784z+28.212 & \dot{m}_{\mathrm{b}}<0\\ 0 & \dot{m}_{\mathrm{b}}=0\\ 5 & \dot{m}_{\mathrm{b}}>0\end{cases}$$

where the first line represents the power consumption of the hydraulic pump at different depths when the buoyancy engine transfers hydraulic oil from the internal tank to the external bladder. The term 5 W is the power required to open the solenoid valve, which allows the hydraulic oil to flow from the external bladder back to the internal tank to increase the net mass. If the buoyancy engine is working, which means $\dot{m}_{\mathrm{b}}\neq 0$, $\dot{m}_{\mathrm{b}}$ is set as ± 0.0015 kg/s. Since the change rate of net mass is not infinite, the target net mass generated by the controller may not be reached immediately.

Based on our experiments, the power that drives the battery to move along the $\boldsymbol{b}_1$ axis is $0.064|\theta|+1.43$ W, whereas the power necessary for rotation along the $\boldsymbol{b}_2$ axis is approximately 5 W. Hence, the power of the attitude regulator can be expressed as follows:

$$P_{\mathrm{p}}=\begin{cases}0.064|\theta|+1.43+5 & \dot{r}_{\mathrm{p1}}\neq 0\ \&\ \dot{\zeta}\neq 0\\ 0.064|\theta|+1.43 & \dot{r}_{\mathrm{p1}}\neq 0\ \&\ \dot{\zeta}=0\\ 5 & \dot{r}_{\mathrm{p1}}=0\ \&\ \dot{\zeta}\neq 0\\ 0 & \dot{r}_{\mathrm{p1}}=0\ \&\ \dot{\zeta}=0\end{cases}$$

where $\dot{r}_{\mathrm{p1}}$ and $\dot{\zeta}$ are set as as ± 0.001 m/s and ± π/36 rad/s, respectively, when the attitude regulator is working. Since the change rate of position is constant and not infinite, the target position of the battery pack may not be reached immediately, which means that the battery pack will be moved from the current to desired location over a period of time.

For the CND system, an altimeter and a controller board are considered. The average power of the altimeter is measured to be 1.92 W, while the controller board consumes approximately 2 W. Consequently, the total average power of the CND system, denoted as P_{CND}, amounts to 3.92 W.

During the case study, several practical considerations were taken into account, and the simulation was adjusted accordingly. These considerations include:

(1) When a glider controlled by LQR is switching from descending to ascending, a large state error yields an exaggerated control input, which will then cause severe oscillations in the state variables. To avoid this, during the switching process the LQR will be deactivated and the actuators will run with inputs only from the feedforward control.

(2) Each actuator has a physical limit. The saturation will occur when the controller requests an actuator to exceed its physical limit. Let subscripts '_tag' denote the target control input generated by the controller. In this study, the physical limits of individual control inputs include:

$$\text{Control input limit}\begin{cases}|m_{\mathrm{b}}|\le 0.714\ \text{kg}\\ 0.02\ \text{m}\ \le r_{\mathrm{p1}}\le 0.144\ \text{m}\\ |\zeta|\le\dfrac{\pi}{3}\ \text{rad}\end{cases}$$

(3) To minimise energy consumption, underwater gliders only enable the control systems when the errors go above certain thresholds. In this paper, LQR control will be triggered when the absolute differences go beyond the below thresholds:

$$\text{LQR trigger condition} \begin{cases} \left| m_{\mathrm{b}} - m_{\mathrm{b_tag}} \right| \geq 0.01 \text{ kg} \\ \left| r_{\mathrm{p1}} - r_{\mathrm{p1_tag}} \right| \geq 0.02 \text{ m} \\ \left| \zeta - \zeta_{\mathrm{_tag}} \right| \geq \pi/36 \text{ rad} \end{cases}$$

(4) For a glider under open-loop control (without LQR), the net mass generated by the feedforward controller without considering the water density gradient may not be enough to drive the glider to the target depth, which is shown in Fig. 9. Therefore, when performing simulations for the glider under open-loop control, the feedforward controller will calculate the net mass by considering the water density at the target depth z_{tag} to ensure the diving depth. According to the Eqs. (16) and (41), the net mass under open-loop control can be expressed as follows:

$$m_{\mathrm{bd}} = \frac{V_{\mathrm{d}}^{\,2}}{g}\left(-\left(K_{\mathrm{D0}} + K_{\mathrm{D}}\alpha_{\mathrm{d}}^{\,2}\right)\sin\gamma_{\mathrm{d}} + \left(K_{\mathrm{L0}} + K_{\mathrm{L}}\alpha_{\mathrm{d}}\right)\cos\gamma_{\mathrm{d}}\right) + \rho(z)\left(\frac{m_{\mathrm{s}} + m_{\mathrm{p}}}{p_5} - K_{\mathrm{vh}} z_{\mathrm{tag}}\right) - \left(m_{\mathrm{s}} + m_{\mathrm{p}}\right)$$

But the net mass for the glider under LQR is still calculated using the local water density to avoid the overestimated net mass target.

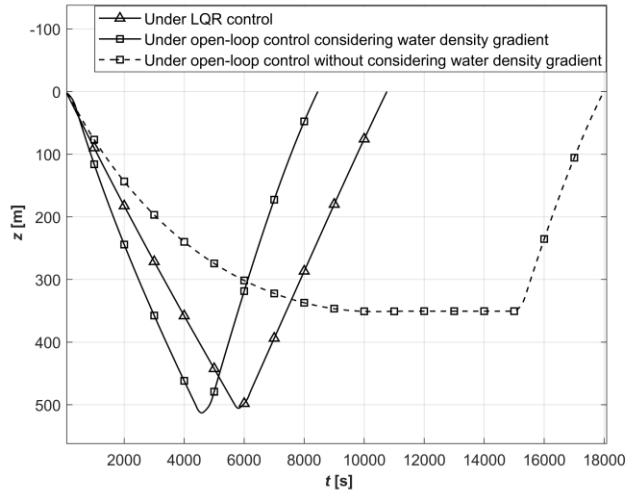

Fig. 9. Diving depth under LQR control and open-loop control with and without considering water density gradient. The net mass generated by the feedforward controller without considering the water density gradient is not able to drive the underwater glider to the target depth (500 m) in the maximum descending time (15,000 s).

In this case study, the control cycle of LQR is set to 1 s. Higher or lower sampling rates can be utilized depending on the specific system requirements. Finally, the $\boldsymbol{Q}$ and $\boldsymbol{R}$ matrices are defined as follows:

$$\boldsymbol{Q}_{\mathrm{_vtc}} = diag\left[20,\ 0.1,\ 0.1,\ 5\right]$$

$$\boldsymbol{R}_{\mathrm{_vtc}} = diag\left[5,\ 1\right]$$

$$\boldsymbol{Q}_{\mathrm{_hrz}} = diag\left[1,\ 1,\ 1,\ 1,\ 100\right]$$

$$\boldsymbol{R}_{\mathrm{_vtc}} = 1$$

5.2 Case I: simulation with density gradient

In the initial case study, the focus is on investigating the performance of the LQR controller under the influence of changing water density. The simulations consider only the density gradient, as defined in Eq. (17) and detailed in Table D-4. Since the underwater glider under open-loop control lacks the ability to adjust the heading angle, both the target and initial heading angles are set to 0 degrees (North). Table 2 presents the variable parameters and their respective ranges utilized in the simulations. It is important to note that the desired velocity and pitch angle (without the "absolute" prefix for convenience) are symmetric during both descending and ascending phases. The energy-accuracy results obtained from these simulations are depicted in Fig. 10.

Table 2 Variable parameters and their ranges

Parameter	Description	Range
z_{tag}	Target diving depth	[200, 400, …, 800] m
$\lvert\theta_{\text{d}}\rvert$	Desired absolute pitch angle	[20, 25, …, 45] deg
V_{d}	Desired gliding velocity	[0.25, 0.3, 0.35, 0.4] m/s

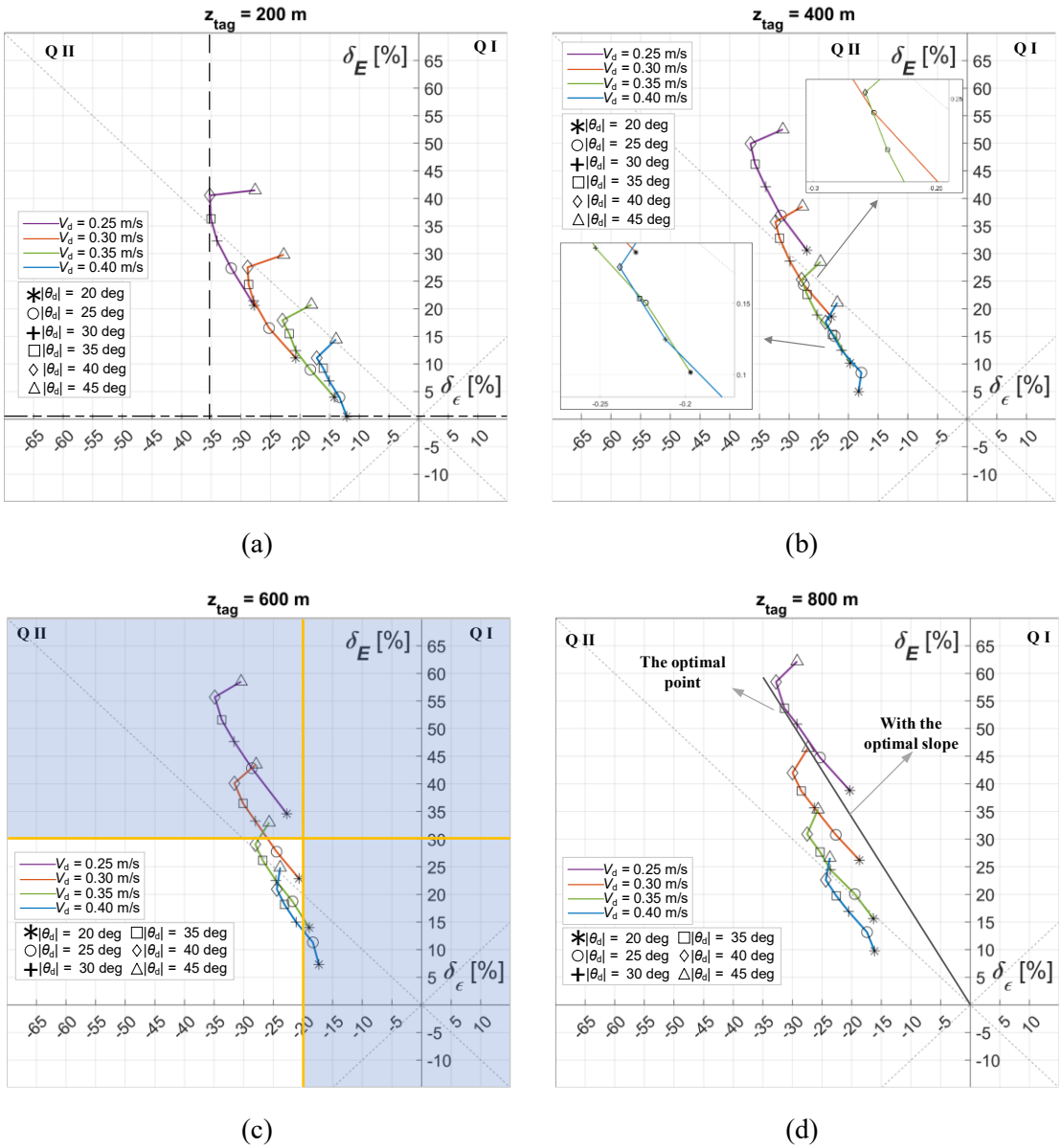

Fig. 10. Gliding velocity contour lines without ocean currents.

• **Overall performance of LQR control**

In Fig. 10, all data points are distributed in the QII indicating that under the given simulation conditions, the LQR controller proves effective in improving motion accuracy at the expense of increased energy consumption. To further analyse the results, two dotted grey lines with slopes of 1 and -1 are utilized to assess the trend of the controller performance. It can be observed that as the depth increases, all curves shift upwards and goes above the line with the slope of -1, which suggests that with increased energy consumption, the motion accuracy cannot be significantly improved. This raises the question of whether the implementation of LQR is necessary for missions in large water depths. For the deeper dives in a steady condition, gliders operate for longer times with low disturbance. Hence, the effect of LQR control is not prominent in such scenarios.

The depicted figure also provides insight into the theoretical limit of the controller's performance. In particular, referring to Fig. 10 (a), the vertical dash line intersecting with the leftmost point signifies the upper limit for enhancing accuracy. Consequently, if the glider is required to perform position/motion accurate missions in 200 m, it is advisable to glide at a velocity of 0.25 m/s with a pitch angle of 40 deg. On the other hand, if the primary objective is to achieve the most energy-efficient glide, it is recommended to glide at 0.4 m/s with a pitch angle of 20 deg. Thus, the method illustrated in the figure can be employed to support the decision-making process for underwater glider operations. It becomes apparent that different mission requirements can lead to significant variations in the operational strategy, highlighting the importance of tailoring the glider's parameters based on specific objectives.

Furthermore, following the method above, if the operation requirement is specified, i.e. 600 m depth, minimum 20% accuracy enhancement, maximum 30% energy consumption increment, the vehicle can identify the potential operation strategies quickly and execute the mission within the specified constraints. It can be seen in Fig. 10 (c) that the horizontal and vertical solid yellow lines represent the acceptable limits of energy consumption increase and motion accuracy improvement (error reduction), respectively. Points distributed within the blue area fail to meet the mission requirements and should be excluded from consideration.

• **Optimum pitch angle at a given velocity**

On certain expeditions, an underwater glider needs to maintain a specific cruise velocity to ensure the quality of the data collected by the sensors. To optimise the energy consumption while maintaining motion accuracy, it becomes crucial to identify the optimum pitch angle. As shown in Fig.10, it is evident that at the same velocity, the pitch angle has a significant impact on both the energy consumption (δ_E) and motion accuracy (δ_ε). Scrutinizing the result as shown in Fig.11, it is observed that the pitch angle directly influences the driving mass. This is attributed to the variation in hydrodynamic forces at different pitch angles, leading to different angles of attack.

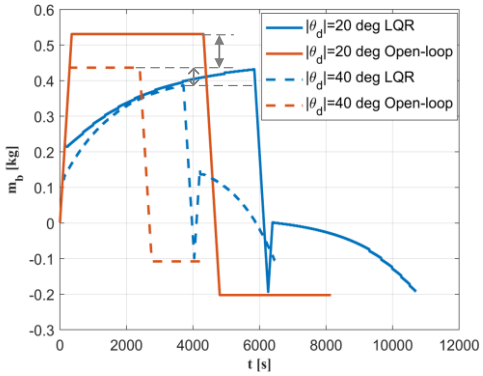

Fig. 11. Driven mass under LQR and open-loop control

(Target depth = 600 m, desired gliding velocity = 0.3 m/s)

This leads to a thinking that an outperforming/efficient controller will consume minimum energy but yield a maximum accuracy enhancement, i.e. accuracy per energy consumption. Therefore, the slope of the tangent line drawn from the origin to the curve represents the optimal point for operation. For instance, in Fig. 10 (d), the grey solid line illustrates the optimal pitch angle of 35 deg under the given condition. In situations where the tangent line cannot be established due to operational constraints and boundaries, the largest negative is preferred as the optimal choice. Table 3 presents the optimal pitch angle at various diving depths and gliding velocities, derived using this approach. y identifying and implementing the optimal pitch angle for specific operational conditions, the underwater glider can achieve a balance between energy efficiency and accuracy enhancement, optimizing its performance for various mission scenarios.

Table 3 The optimal pitch angle at various diving depths and gliding velocities

Gliding velocity [m/s] / Diving depth [m]	0.25	0.30	0.35	0.40
200	20 deg	20 deg	20 deg	20 deg
400	20 deg	20 deg	20 deg	20 deg
600	25 deg	20 deg	20 deg	20 deg
800	35 deg	30 deg	20 deg	20 deg

- **Optimum gliding velocity at a given pitch angle**

Vice versa, some missions require underwater gliders to operate at a specific pitch angle so that the sensors can face the target with a specific angle. Or, underwater gliders need to perform a manoeuvre with a gliding angle for collision avoidance; then pitch angle is an effective variable to achieve this. Under these circumstances, the gliding velocity can be optimized for the controller.

The same method can be applied to optimize the gliding velocity while maintaining a specific pitch angle. As depicted in Figure 12, the data is presented in curves representing different pitch angles. But since the gliding velocity is a dominant factor (Javaid et al., 2016), at a higher velocity the LQR will all consume less energy for better accuracy. By employing the slope analysis method, we can find that at the same pitch angle the optimum velocity is always the highest velocity. Therefore, for high-speed gliding missions, the LQR controller becomes even more crucial in achieving optimal performance.

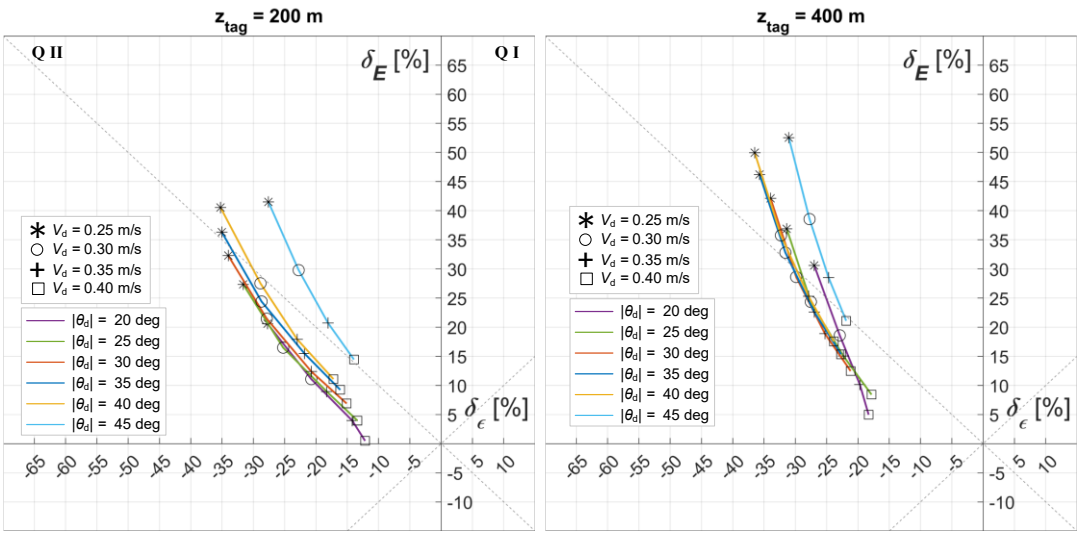

(a) (b)

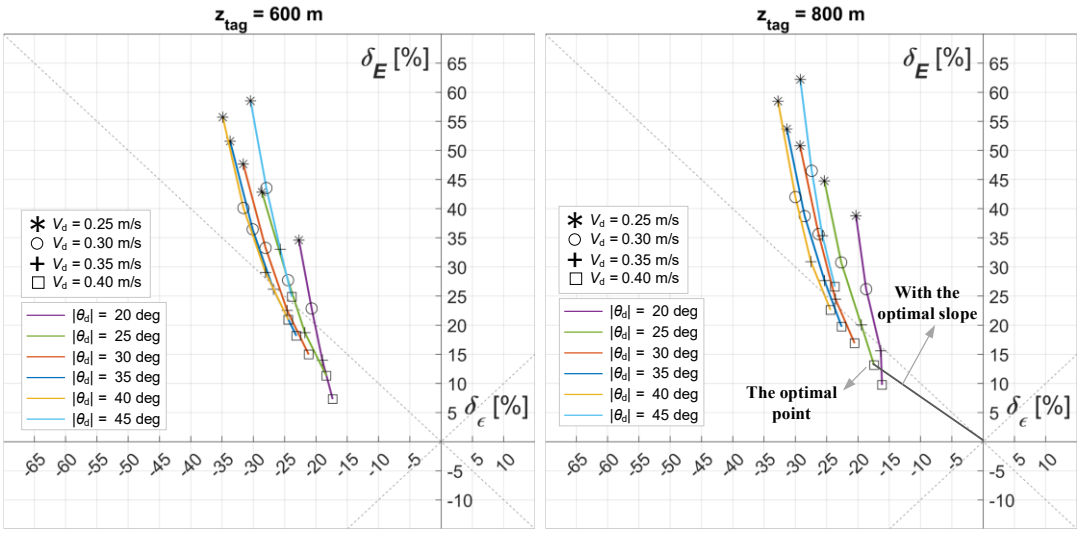

(c) (d)

Fig. 12. Pitch angle contour with the density gradient.

5.3 Case II: simulation combining density gradient with ocean currents

In addition to the seawater density gradient, vortex flow in the ocean is a challenging scenario for underwater gliders, and it is a common occurrence in the ocean. Among different scales of ocean eddies, submesoscale eddies with 100 m ~10 km in size pose the most significant impact on underwater glider operation.

A vortex centred at the origin of the inertial frame I_0 is modelled to further investigate the performance of the developed LQR controller. The vortex represents a steady and ununiform flow field characterized by the following velocity profile:

$$\boldsymbol{V}_{\mathrm{f}}(\boldsymbol{b}) = \frac{H}{2\pi\left(x^2+y^2+z^2\right)}\left[-y,\, x,\, 0\right]^{\mathrm{T}} \text{ m/s}$$

where H is the intensity of the vortex. In the simulations, H will be kept at 100 m^2/s. Figure 13 shows the vortex velocity in the inertial frame.

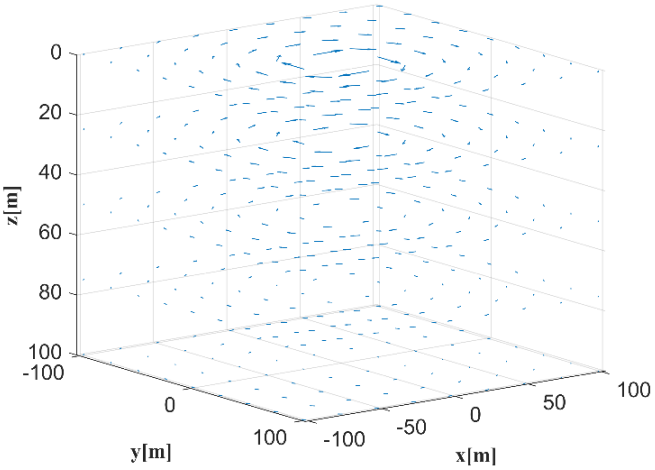

Fig. 13. Velocity of submesoscale eddy with intensity 100 m^2/s.

To prevent the denominator ($x^2+y^2+z^2$) from being zero in the vortex velocity calculation, we set the initial position of the glider in the simulations to $x = y = z = 0.1$ m. Additionally, both the desired heading angle and initial heading angle are set to 0 for consistency. The simulations are then performed using variable parameters within the defined ranges outlined in Table 1. The results are shown in Fig. 14.

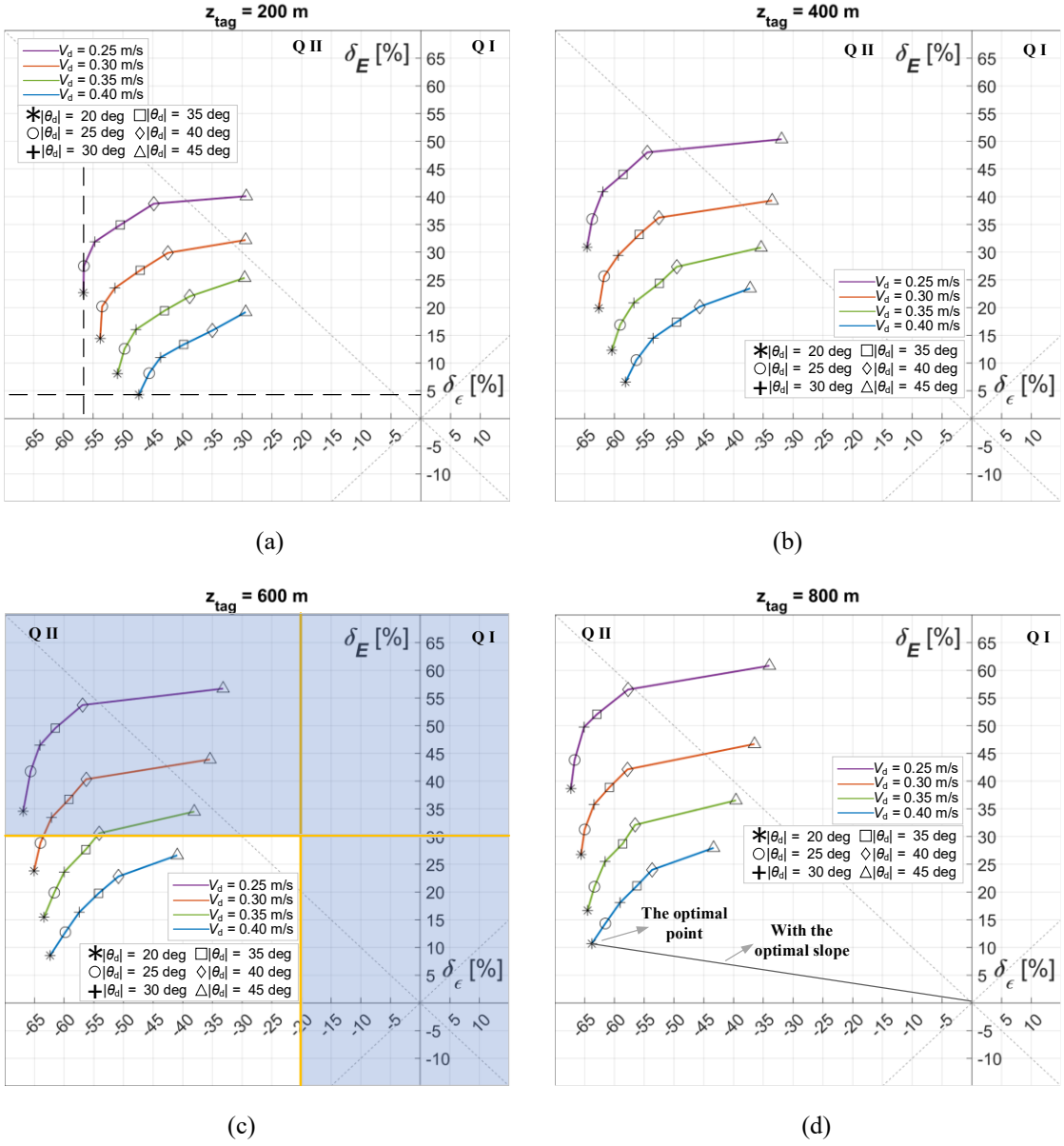

Fig. 14. Gliding velocity contour lines with a vortex.

- **Overall performance of LQR control**

First, all data points are distributed in the QII but are significantly shifted to the left compared to the results in Fig. 10, indicating that LQR yields a much more observable accuracy improvement under the disturbance of the modelled vertex flow. The distributions and the trends of the data point remain consistent across the ranging water depth. With the increase of water depth, the curves slightly shift towards upper left, which is contrary to the obvious upward shift observed in Fig. 10. These results suggest that the LQR control becomes even more crucial in underwater glider operations influenced by vortex flows, particularly in deeper water conditions.

As described before and exemplified in Fig. 14 (a), the upper limits of the LQR controller are investigated at different depths and summarized in Tables 4 and 5. Across various diving depths, the maximum motion accuracy improvement always occurs at the lowest gliding velocity of 0.25 m/s and the lowest pitch angle of 20 deg. The maximum motion accuracy improvement increases with the depth. On the other hand, the minimum energy consumption can be achieved by maximising the gliding speed and minimising the pitch angle. Furthermore, as shown in Fig. 14 (c), if the same thresholds have been set as in the previous section, a large number of operations cannot be performed due to the presence of ocean flow.

Table 4 The maximum motion accuracy of improvement and the corresponding gliding velocity and pitch angle at different diving depths with the vortex

Diving depth [m]	Maximum motion accuracy improvement (max $\lvert\delta_\varepsilon\rvert$) [%]	Gliding velocity [m/s]	Pitch angle [deg]
200	56.64	0.25	20
400	64.59	0.25	20
600	66.90	0.25	20
800	67.30	0.25	20

Table 5 The minimum energy consumption increase and the corresponding gliding velocity and pitch angle at different diving depths with the vortex

Diving depth [m]	Minimum energy consumption increase (Min δ_E) [%]	Gliding velocity [m/s]	Pitch angle [deg]
200	4.31	0.4	20
400	6.60	0.4	20
600	8.55	0.4	20
800	10.68	0.4	20

- **Optimum pitch angle at a given velocity**

From Fig. 14, we can find that with the same target depth and gliding velocity, both δ_E and δ_ε increase as the pitch angle increases, which indicates that the performance of LQR deteriorates with larger pitch angles. The reason for the increase in δ_E is the same as when there is no ocean current, while the reason for δ_ε can be revealed in Fig. 15. It is observed that the LQR controller is capable of correcting the heading angle; however, when using smaller pitch angles, a larger correction is required to maintain the desired heading.

Furthermore, employing the same slope analysis method as described in Section 5.2 and exemplified in Fig. 14 (d), we can find that the optimal pitch angle for maximizing accuracy per energy is always the smallest one.

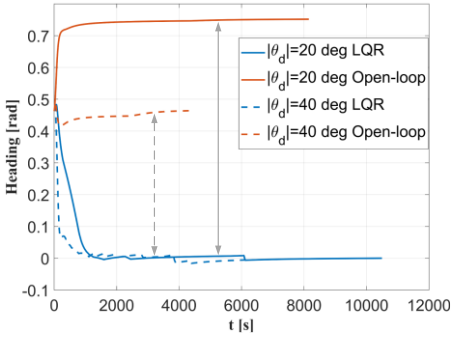

Fig. 15. Heading angle under LQR and open-loop control.

(Target depth = 600 m, desired gliding velocity = 0.3 m/s, desired heading = 0 rad)

- **Optimum gliding velocity at a given pitch angle**

The pitch angle contour lines are presented in Fig. 16. One trend that can be observed is that with the given target depth and pitch angle, more energy is needed for higher pitch angles to improve motion accuracy. Additionally, the glider demonstrates a preference for higher gliding velocities. According to the slope analysis, the optimal gliding velocity for minimizing energy cost per accuracy is consistently the highest velocity, which in this specific simulation is 0.4 m/s.

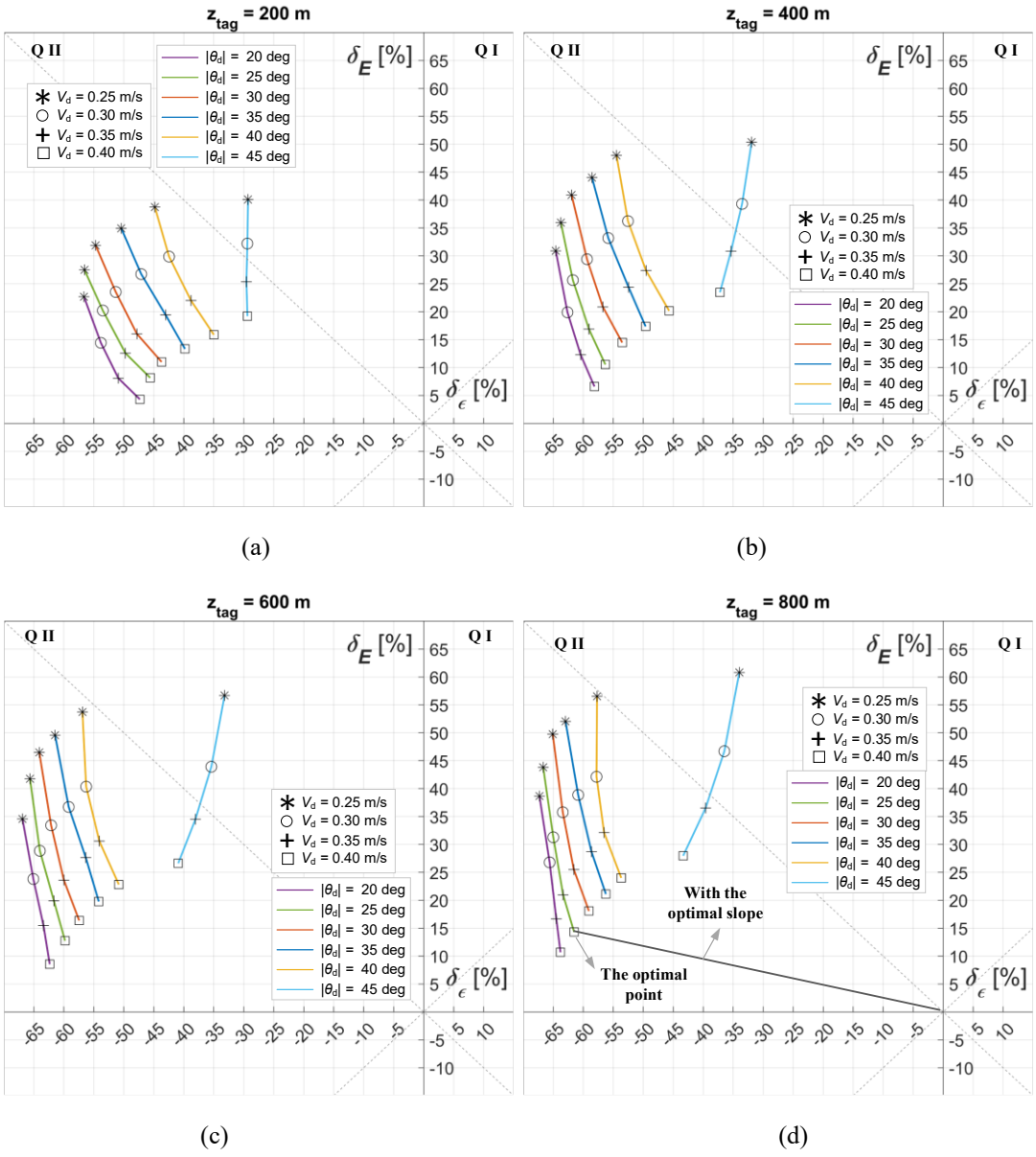

Fig. 16. Pitch angle contour lines with a vortex.

6 Energy-accuracy chart and the quadrant analysis

According to the above result discussion of the case study, we introduce the quadrant analysis to support the decision-making process for underwater gliders to perform energy-efficient and motion-precise operations. Here we present a recommended procedure and the potential benefits of the use of energy-accuracy charts.

(1) **Overall evaluation of the controller effectiveness:** The overall evaluation determines whether the developed controller can effectively control the vehicle or not. It can be evaluated based on the quadrant distribution of the results in the energy-accuracy chart. For the controller targeting the improvement of the motion accuracy, results distributed in QII and QIII are acceptable. Whereas for the controller with the objective to reduce energy consumption, results distributed in QIII and QIV are acceptable. QI is not acceptable under any condition.
(2) **Trend analysis**: In a quadrant chart, lines with slopes of 1 and -1 can be used to evaluate the trend of LQR in terms of energy consumption and motion accuracy. If the result tends to be aligned close to the δ_ε axis, the controllers are more effective in enhancing motion accuracy. Vice versa, it tends to consume more energy with minimum improvement in energy consumption.
(3) **Optimum identifications with the tangent line slope analysis**: Gliding velocity and pitch angle contour lines in the quadrant chart can be employed to investigate the controller performance under the different requirements. Energy cost per accuracy improvement is a key performance indicator to quantify the controller performance. The slope of the line connecting each point to the origin quantifies this performance. The tangent line from the origin to the resulting curve (if exists within the range of the investigation) is the extreme point for the energy per accuracy indicator. Using this analysis, the optimal operational strategy for the best value of energy can be quickly identified.
(4) **Vehicle operational preference, controller performance and limitation:** Underwater gliders have versatile operational profiles and requirements. Therefore to compare different vehicles or controllers or to select a suitable underwater glider for a specific mission, this chart can be used. It can identify the preference of the vehicles or the controllers as well as the limits.

Based on the above analysis, the balance between energy consumption and motion accuracy of the underwater glider under feedback control can be effectively achieved.

7 Conclusions

In this paper, a fully coupled dynamics-energy-control model for underwater gliders has been established. A novel evaluation framework for assessing energy consumption and motion accuracy under feedback control is proposed. The following key conclusions can be drawn from this study:

1. A 6 DOF dynamics model of the underwater glider considering seawater density gradient and submesoscale eddies is established based on the Newton-Euler equations. The dynamics model is then linearized, and a new controller combining feedforward and LQR controls in both the vertical and horizontal planes is developed.
2. Then, the energy consumption model and the motion accuracy evaluation method under feedback control are proposed. The non-dimensional energy consumption and motion accuracy are presented. Based on this, the energy-accuracy chart can be obtained to explain the relationship between energy consumption and motion accuracy.
3. Two case studies in ocean environmental conditions are conducted using the Petrel-II underwater glider. The performance has been evaluated in various operating conditions under different mission requirements. The quadrant chart analysis can quickly help to identify the optimum operational strategy with quantitative support for decision making. Moreover, the concept of the optimal cost energy for motion accuracy is proposed which can be obtained by the slope analysis.
4. The proposed energy-accuracy evaluation method is summarised and recommended to be used to assess the glider with respect to specific missions to effectively balance and optimize the performance on energy consumption and motion accuracy.

In the near future, the researcher will further develop the method to implement and evaluate different controllers (such as proportional–integral–derivative, PID) to contribute to the design and development of novel, efficient and precise underwater gliders.

Acknowledgments

The funding supports received from the National Key R&D Program of China, the National Natural Science Foundation of China (Grant: 11902219), the Natural Science Foundation of Tianjin City (Grant 18JCJQJC46400), the Royal Society (Biomimetic improvement for the hydrodynamic performance of the enduring underwater glider, Ref: IEC\NSFC\201050), the Shuimu Scholar Program of Tsinghua University (Grant: 2022SM018), and the China Scholarship Council (File No. 202006250118) are greatly appreciated and acknowledged.

The authors also would like to express their sincere thanks to Callum Stark for his helping to revise the grammar.

References

Cao, J., Cao, J., Zeng, Z., Lian, L., 2016a. Nonlinear multiple-input-multiple-output adaptive backstepping control of underwater glider systems. International Journal of Advanced Robotic Systems 13 (6).

Cao, J., Cao, J., Zeng, Z., Lian, L., 2016b. Optimal path planning of underwater glider in 3D dubins motion with minimal energy consumption, OCEANS 2016 - Shanghai, pp. 1-7.

Eriksen, C.C., Osse, T.J., Light, R.D., Wen, T., Lehman, T.W., Sabin, P.L., Ballard, J.W., Chiodi, A.M., 2001. Seaglider: a long-range autonomous underwater vehicle for oceanographic research. IEEE Journal of Oceanic Engineering 26 (4), 424-436.

Falcão Carneiro, J., Gomes de Almeida, F., 2016. Model of a thermal driven volumetric pump for energy harvesting in an underwater glider. Energy 112, 28-42.

Falcão Carneiro, J., Gomes de Almeida, F., 2018. Model and simulation of the energy retrieved by thermoelectric generators in an underwater glider. Energy Conversion and Management 163, 38-49.

Fan, S., Woolsey, C.A., 2014. Dynamics of underwater gliders in currents. Ocean Engineering 84, 249-258.

Field, M., Beguery, L., Oziel, L., Gascard, J.C., 2015. Barents Sea monitoring with a SEA EXPLORER glider, OCEANS 2015 - Genova. IEEE, Genova, pp. 1-5.

Fossen, T.I., 2011. Handbook of Marine Craft Hydrodynamics and Motion Control. John Wiley & Sons.

Hamid, N.A., Ismail, I.S., Yunus, N., Jali, M.N., Rosly, A.S., 2022. Taxpayer Perceptions of tax awareness, tax education, and tax complexity among small and medium enterprises in Malaysia: A quadrant analysis approach. Universal Journal of Accounting and Finance 10 (1), 231-242.

Isa, K., Arshad, M.R., Ishak, S., 2014. A hybrid-driven underwater glider model, hydrodynamics estimation, and an analysis of the motion control. Ocean Engineering 81, 111-129.

Jantapremjit, P., K.Daengchart, Wilson, P.A., 2020. Modelling and control of an underwater glider. Journal of Research and Applications in Mechanical Engineering 9 (1), 13.

Javaid, M.Y., Ovinis, M., Hashim, F.B.M., Maimun, A., Ali, S.S.A., Ahmed, S.A., 2016. Investigation on the dynamic stability of an underwater glider using CFD simulation, 2016 IEEE International Conference on Underwater System Technology: Theory and Applications (USYS), pp. 230-235.

Jing, G., Lei, L., Gang, Y., 2022. Dynamic modeling and experimental analysis of an underwater glider in the ocean. Applied Mathematical Modelling 108, 392-407.

Joo, M.G., Qu, Z., 2015. An autonomous underwater vehicle as an underwater glider and its depth control. International Journal of Control, Automation and Systems 13 (5), 1212-1220.

Lei, L., Zhou, Y., Yang, G., 2023. Multisource information fusion-based environment perception and dynamic model of underwater vehicle in irregular ocean environment. Information Fusion 94, 257-271.

Leonard, N.E., Graver, J.G., 2001. Model-based feedback control of autonomous underwater gliders. IEEE Journal of Oceanic Engineering 26 (4), 633-645.

Ma, Z., Wang, Y., Wang, S., Yang, Y., 2016. Ocean thermal energy harvesting with phase change material for underwater glider. Applied Energy 178, 557-566.

Mangan, M.R., Oldroyd, H.J., Paw U, K.T., Clay, J.M., Drake, S.A., Kelley, J., Suvočarev, K., 2022. Integrated Quadrant Analysis: A New Method for Analyzing Turbulent Coherent Structures. Boundary-Layer Meteorology 184 (1), 45-69.

Noh, M.M., Arshad, M.R., Mokhtar, R.M., 2011. Depth and pitch control of USM underwater glider: Performance comparison PID vs. LQR.

Ramos, A.G., Garcia-Garrido, V.J., Mancho, A.M., Wiggins, S., Coca, J., Glenn, S., Schofield, O., Kohut, J., Aragon, D., Kerfoot, J., Haskins, T., Miles, T., Haldeman, C., Strandskov, N., Allsup, B., Jones, C., Shapiro, J., 2018. Lagrangian coherent structure assisted path planning for transoceanic autonomous underwater vehicle missions. Sci Rep 8 (1), 4575.

Sherman, J., Davis, R.E., Owens, W.B., Valdes, J., 2001. The autonomous underwater glider "Spray". IEEE Journal of Oceanic Engineering 26 (4), 437-446.

Song, Y., Wang, Y., Yang, S., Wang, S., Yang, M., 2020. Sensitivity analysis and parameter optimization of energy consumption for underwater gliders. Energy 191.

Song, Y., Xie, X., Wang, Y., Yang, S., Ma, W., Wang, P., 2021a. Energy consumption prediction method based on LSSVM-PSO model for autonomous underwater gliders. Ocean Engineering 230.

Song, Y., Ye, H., Wang, Y., Niu, W., Wan, X., Ma, W., 2021b. Energy Consumption Modeling for Underwater Gliders Considering Ocean Currents and Seawater Density Variation. Journal of Marine Science and Engineering 9 (11).

Stommel, H., 1989. The Slocum Mission. Oceanography 2 (1), 22-25.

Su, S., Wang, N., 2022. Offshore Robotics. Springer.

Sun, C., Tian, J., Huang, R., Dong, H., Li, H., Ma, Y., 2023. Internal layout optimization of the blended-wing-body underwater glider based on a range target. Ocean Engineering 280, 114450.

Tchilian, R.d.S., Rafikova, E., Gafurov, S.A., Rafikov, M., 2017. Optimal Control of an Underwater Glider Vehicle. Procedia Engineering 176, 732-740.

Thomasson, P.G., 2000. Equations of Motion of a Vehicle in a Moving Fluid. Journal of Aircraft 37 (4), 630-639.

Ullah, B., Ovinis, M., Baharom, M.B., Ali, S.S.A., Javaid, M.Y., 2018. Pitch and Depth Control of Underwater Glider using LQG and LQR via Kalman Filter. International Journal of Vehicle Structures and Systems 10 (2).

Ullah, B., Ovinis, M., Baharom, M.B., Javaid, M.Y., Izhar, S.S., 2015. Underwater gliders control strategies: A review, 2015 10th Asian Control Conference (ASCC), pp. 1-6.

Wang, J., Wu, Z., Dong, H., Tan, M., Yu, J., 2022. Development and Control of Underwater Gliding Robots: A Review. IEEE/CAA Journal of Automatica Sinica 9 (9), 1543-1560.

Wang, S., Sun, X., Wang, Y., Wu, J., Wang, X., 2011. Dynamic modeling and motion simulation for a winged hybrid-driven underwater glider. China Ocean Engineering 25 (1), 97-112.

Wang, Y., Zhang, H., Wang, S., 2009. Trajectory Control Strategies for the Underwater Glider, 2009 International Conference on Measuring Technology and Mechatronics Automation, pp. 918-921.

Wang, Y., Zhang, Y., Wang, L., Li, Z., Ma, Z., Zhang, C., Chang, L., Wang, J., Ma, W., 2023. Modeling and performance analysis of underwater gliders based on the virtual prototype technology. Ocean Engineering 281, 114763.

Webb, D.C., Simonetti, P.J., Jones, C.P., 2001. SLOCUM: an underwater glider propelled by environmental energy. IEEE Journal of Oceanic Engineering 26 (4), 447-452.

Woolsey, C.A., 2011. Vehicle Dynamics in Currents. Virginia Center for Autonomous Systems, p. 29.

Wu, H., Niu, W., Wang, S., Yan, S., 2021a. Multi-objective optimization for control parameters of underwater gliders considering effect of uncertain input errors. Proceedings of the Institution of Mechanical Engineers, Part C: Journal of Mechanical Engineering Science 236 (6), 3093-3110.

Wu, H., Niu, W., Wang, S., Yan, S., 2021b. An optimization method for control parameters of underwater gliders considering energy consumption and motion accuracy. Applied Mathematical Modelling 90, 1099-1119.

Wu, H., Niu, W., Wang, S., Yan, S., 2022. A feedback control strategy for improving the motion accuracy of underwater gliders in currents: Performance analysis and parameter optimization. Ocean Engineering 252.

Wu, H., Niu, W., Zhang, Y., Wang, S., Yan, S., 2023. A hybrid polynomial-based optimization method for underwater gliders with parameter uncertainty. Applied Ocean Research 133, 103486.

Yan, Y., Zhou, X., Chu, Z., Stell, L., Shariati, M.A., Wang, R.K., Liao, Y.J., 2021. Topographic quadrant analysis of peripapillary superficial microvasculature in optic disc drusen. Frontiers in Neurology 12, 666359.

Yang, Y., Liu, Y., Wang, Y., Zhang, H., Zhang, L., 2017. Dynamic modeling and motion control strategy for deep-sea hybrid-driven underwater gliders considering hull deformation and seawater density variation. Ocean Engineering 143, 66-78.

Yu, J., Zhang, F., Zhang, A., Jin, W., Tian, Y., 2013. Motion Parameter Optimization and Sensor Scheduling for the Sea-Wing Underwater Glider. IEEE Journal of Oceanic Engineering 38 (2), 243-254.

Appendix A:

In the inertial frame, according to Euler's first and second axioms, we have

$$\dot{\boldsymbol{p}} = \sum_{i=1}^{I} \boldsymbol{f}_{\mathrm{ext}_i} \tag{A1}$$

$$\dot{\boldsymbol{\pi}} = \sum_{i=1}^{I} \left(\boldsymbol{l}_i \times \boldsymbol{f}_{\mathrm{ext}_i} \right) + \sum_{j=1}^{J} \boldsymbol{\tau}_{\mathrm{ext}_j} \tag{A2}$$

where $\boldsymbol{p}$ is the translational momentum of the glider in the inertial frame, $\boldsymbol{\pi}$ is the angular momentum of the glider in the inertial frame, $\boldsymbol{f}_{\mathrm{ext}_i}$ is the external force applied to the glider, $\boldsymbol{l}_i$ is the vector from I_0 to $\boldsymbol{f}_{\mathrm{ext}_i}$, $\boldsymbol{\tau}_{\mathrm{ext}_j}$ is the external torque acting on the glider, I is the number of external forces, and J is the number of pure external torque.

The translational momentum and angular momentum of the glider in the inertial frame can be expressed in the body frame as

$$\boldsymbol{p} = \boldsymbol{R}_{\mathrm{B}}^{\mathrm{I}} \boldsymbol{P} \tag{A3}$$

$$\boldsymbol{\pi} = \boldsymbol{R}_{\mathrm{B}}^{\mathrm{I}} \boldsymbol{\Pi} + \boldsymbol{b} \times \boldsymbol{p} \tag{A4}$$

where $\boldsymbol{P}$ and $\boldsymbol{\Pi}$ are the translational and angular momentums of the glider in the body frame, respectively.

Differentiating Eqs. (A3) and (A4) again time, results in:

$$\dot{\boldsymbol{p}} = \boldsymbol{R}_{\mathrm{B}}^{\mathrm{I}} \left(\dot{\boldsymbol{P}} + \boldsymbol{\omega} \times \boldsymbol{P} \right) \tag{A5}$$

$$\dot{\boldsymbol{\pi}} = \boldsymbol{R}_{\mathrm{B}}^{\mathrm{I}} \left(\dot{\boldsymbol{\Pi}} + \boldsymbol{\omega} \times \boldsymbol{\Pi} \right) + \boldsymbol{R}_{\mathrm{B}}^{\mathrm{I}} \boldsymbol{v} \times \boldsymbol{p} + \boldsymbol{b} \times \dot{\boldsymbol{p}} \tag{A6}$$

Substituting Eqs. (A1) and (A2) into Eqs. (A5) and (A6) gives:

$$\dot{\boldsymbol{P}} = \boldsymbol{P} \times \boldsymbol{\omega} + \boldsymbol{R}_{\mathrm{I}}^{\mathrm{B}} \sum_{i=1}^{I} \boldsymbol{f}_{\mathrm{ext}_i} \tag{A7}$$

$$\dot{\boldsymbol{\Pi}} = \boldsymbol{\Pi} \times \boldsymbol{\omega} + \boldsymbol{P} \times \boldsymbol{v} + \boldsymbol{R}_{\mathrm{I}}^{\mathrm{B}} \left(\sum_{i=1}^{I} \left(\boldsymbol{l}_i - \boldsymbol{b} \right) \times \boldsymbol{f}_{\mathrm{ext}_i} \right) + \boldsymbol{R}_{\mathrm{I}}^{\mathrm{B}} \sum_{j=1}^{J} \boldsymbol{\tau}_{\mathrm{ext}_j} \tag{A8}$$

According to Eq. (26) , Eqs. (A7) and (A8) can be then expressed as

$$\dot{\boldsymbol{P}} = \boldsymbol{P} \times \boldsymbol{\omega} + \boldsymbol{F}_{\mathrm{ext}} \tag{A9}$$

$$\dot{\boldsymbol{\Pi}} = \boldsymbol{\Pi} \times \boldsymbol{\omega} + \boldsymbol{P} \times \boldsymbol{v} + \boldsymbol{T}_{\mathrm{ext}} \tag{A10}$$

To obtain the translational momentum $\boldsymbol{P}$ and angular momentum $\boldsymbol{\Pi}$, we first calculate the kinetic energy of the glider, which is equal to the sum of the kinetic energies of each part.

The kinetic energy of the static mass is

$$T_{\mathrm{s}} = \frac{1}{2} m_{\mathrm{s}} \left\| \boldsymbol{v}_{\mathrm{s}} \right\|^2 + \frac{1}{2} \boldsymbol{\omega}_{\mathrm{s}}^{\mathrm{T}} \boldsymbol{J}_{\mathrm{s}} \boldsymbol{\omega}_{\mathrm{s}} = \frac{1}{2} \begin{bmatrix} \boldsymbol{v} \\ \boldsymbol{\omega} \end{bmatrix}^{\mathrm{T}} \boldsymbol{M}_{\mathrm{s}} \begin{bmatrix} \boldsymbol{v} \\ \boldsymbol{\omega} \end{bmatrix} \tag{A11}$$

where $\boldsymbol{M}_{\mathrm{s}}$ is the generalized inertia matrixes of static mass. Let $\boldsymbol{I}$ and $\boldsymbol{J}_{\mathrm{s}}$ donate a 3×3 identity matrix and the inertia matrixes of m_{s} with respect to body frame coordinates, respectively, $\boldsymbol{M}_{\mathrm{s}}$ can be expressed as

$$\boldsymbol{M}_{\mathrm{s}}=\begin{bmatrix} m_{\mathrm{s}}\boldsymbol{I} & -m_{\mathrm{s}}\hat{\boldsymbol{r}}_{\mathrm{s}} \\ m_{\mathrm{s}}\hat{\boldsymbol{r}}_{\mathrm{s}} & \boldsymbol{J}_{\mathrm{s}} \end{bmatrix}$$

The kinetic energy of the battery pack is

$$T_{\mathrm{p}}=\frac{1}{2}m_{\mathrm{p}}\left\|\boldsymbol{v}_{\mathrm{p}}\right\|^{2}+\frac{1}{2}\boldsymbol{\omega}_{\mathrm{p}}{}^{\mathrm{T}}\boldsymbol{J}_{\mathrm{p}}\boldsymbol{\omega}_{\mathrm{p}}=\frac{1}{2}\begin{bmatrix} \boldsymbol{v} \\ \boldsymbol{\omega} \\ \dot{\boldsymbol{r}}_{\mathrm{p}} \\ \dot{\zeta}\boldsymbol{b}_{1} \end{bmatrix}^{T}\boldsymbol{M}_{\mathrm{p}}\begin{bmatrix} \boldsymbol{v} \\ \boldsymbol{\omega} \\ \dot{\boldsymbol{r}}_{\mathrm{p}} \\ \dot{\zeta}\boldsymbol{b}_{1} \end{bmatrix} \tag{A12}$$

where $\boldsymbol{M}_{\mathrm{p}}$ is the generalized inertia matrixes of the battery pack. Let $\boldsymbol{J}_{\mathrm{p}}$ denote the inertial matrix of the battery pack, $\boldsymbol{M}_{\mathrm{p}}$ can be expressed as

$$\boldsymbol{M}_{\mathrm{p}}=\begin{bmatrix} m_{\mathrm{p}}\boldsymbol{I} & -m_{\mathrm{p}}\hat{\boldsymbol{r}}_{\mathrm{p}} & m_{\mathrm{p}}\boldsymbol{I} & \boldsymbol{0} \\ m_{\mathrm{p}}\hat{\boldsymbol{r}}_{\mathrm{p}} & \boldsymbol{J}_{\mathrm{p}}-m_{\mathrm{p}}\hat{\boldsymbol{r}}_{\mathrm{p}}\hat{\boldsymbol{r}}_{\mathrm{p}} & m_{\mathrm{p}}\hat{\boldsymbol{r}}_{\mathrm{p}} & \boldsymbol{J}_{\mathrm{p}} \\ m_{\mathrm{p}}\boldsymbol{I} & -m_{\mathrm{p}}\hat{\boldsymbol{r}}_{\mathrm{p}} & m_{\mathrm{p}}\boldsymbol{I} & \boldsymbol{0} \\ \boldsymbol{0} & \boldsymbol{J}_{\mathrm{p}} & \boldsymbol{0} & \boldsymbol{J}_{\mathrm{p}} \end{bmatrix}$$

Let $\boldsymbol{J}_{\mathrm{p}}^{0}$ denote the initial inertial matrix when the battery pack is in the stationary state with $\zeta=0$. Then,

$$\begin{cases} \boldsymbol{J}_{\mathrm{p}}=\boldsymbol{R}_{\mathrm{p}}^{\mathrm{b}}\boldsymbol{J}_{\mathrm{p}}^{0}\left(\boldsymbol{R}_{\mathrm{p}}^{\mathrm{b}}\right)^{\mathrm{T}} \\ \boldsymbol{R}_{\mathrm{p}}^{\mathrm{b}}=\begin{bmatrix} 1 & 0 & 0 \\ 0 & \cos\zeta & -\sin\zeta \\ 0 & \sin\zeta & \cos\zeta \end{bmatrix} \end{cases}$$

Since m_b is very small compared to m_{s} and m_{p}, we ignore the kinetic energy of variable ballast here. Then, the total kinetic energy of the glider is

$$T=T_{\mathrm{s}}+T_{\mathrm{p}}=\frac{1}{2}\begin{bmatrix} \boldsymbol{v} \\ \boldsymbol{\omega} \\ \dot{\boldsymbol{r}}_{\mathrm{p}} \\ \dot{\zeta}\boldsymbol{b}_{1} \end{bmatrix}^{\mathrm{T}}\boldsymbol{M}\begin{bmatrix} \boldsymbol{v} \\ \boldsymbol{\omega} \\ \dot{\boldsymbol{r}}_{\mathrm{p}} \\ \dot{\zeta}\boldsymbol{b}_{1} \end{bmatrix} \tag{A13}$$

where

$$\boldsymbol{M}=\begin{bmatrix} \left(m_{\mathrm{s}}+m_{\mathrm{p}}\right)\boldsymbol{I} & -m_{\mathrm{s}}\hat{\boldsymbol{r}}_{\mathrm{s}}-m_{\mathrm{p}}\hat{\boldsymbol{r}}_{\mathrm{p}} & m_{\mathrm{p}}\boldsymbol{I} & \boldsymbol{0} \\ m_{\mathrm{s}}\hat{\boldsymbol{r}}_{\mathrm{s}}+m_{\mathrm{p}}\hat{\boldsymbol{r}}_{\mathrm{p}} & \boldsymbol{J}_{\mathrm{s}}+\boldsymbol{J}_{\mathrm{p}}-m_{\mathrm{p}}\hat{\boldsymbol{r}}_{\mathrm{p}}\hat{\boldsymbol{r}}_{\mathrm{p}} & m_{\mathrm{p}}\hat{\boldsymbol{r}}_{\mathrm{p}} & \boldsymbol{J}_{\mathrm{p}} \\ m_{\mathrm{p}}\boldsymbol{I} & -m_{\mathrm{p}}\hat{\boldsymbol{r}}_{\mathrm{p}} & m_{\mathrm{p}}\boldsymbol{I} & \boldsymbol{0} \\ \boldsymbol{0} & \boldsymbol{J}_{\mathrm{p}} & \boldsymbol{0} & \boldsymbol{J}_{\mathrm{p}} \end{bmatrix}$$

Differentiating total kinetic energy T with respect to the velocity and angular velocity of the glider in the body frame, respectively, we can obtain the translational and angular momentums as follows

$$\boldsymbol{P} = \frac{\partial T}{\partial \boldsymbol{v}} = m_{\mathrm{s}}\left(\boldsymbol{v} + \boldsymbol{\omega} \times \boldsymbol{r}_{\mathrm{s}}\right) + m_{\mathrm{p}}\left(\boldsymbol{v} + \boldsymbol{\omega} \times \boldsymbol{r}_{\mathrm{p}} + \dot{\boldsymbol{r}}_{\mathrm{p}}\right) \tag{A14}$$

$$\boldsymbol{\Pi} = \frac{\partial T}{\partial \boldsymbol{\omega}} = \left(\boldsymbol{J}_{\mathrm{s}} + \boldsymbol{J}_{\mathrm{p}}\right)\boldsymbol{\omega} + m_{\mathrm{s}}\hat{\boldsymbol{r}}_{\mathrm{s}}\boldsymbol{v} + m_{\mathrm{p}}\hat{\boldsymbol{r}}_{\mathrm{p}}\left(\boldsymbol{v} + \boldsymbol{\omega} \times \boldsymbol{r}_{\mathrm{p}} + \dot{\boldsymbol{r}}_{\mathrm{p}}\right) + \boldsymbol{J}_{\mathrm{p}}\dot{\boldsymbol{\zeta}}_{\boldsymbol{b}} \tag{A15}$$

Then, differentiating the translational momentum $\boldsymbol{P}$ and angular momentum $\boldsymbol{\Pi}$ against time, results in

$$\dot{\boldsymbol{P}} = m_{\mathrm{s}}\left(\dot{\boldsymbol{v}} + \dot{\boldsymbol{\omega}} \times \boldsymbol{r}_{\mathrm{s}}\right) + m_{\mathrm{p}}\left(\dot{\boldsymbol{v}} + \dot{\boldsymbol{\omega}} \times \boldsymbol{r}_{\mathrm{p}} + \boldsymbol{\omega} \times \dot{\boldsymbol{r}}_{\mathrm{p}} + \ddot{\boldsymbol{r}}_{\mathrm{p}}\right) \tag{A16}$$

$$\begin{aligned}\dot{\boldsymbol{\Pi}} = {} & \dot{\boldsymbol{J}}_{\mathrm{p}}\boldsymbol{\omega} + \left(\boldsymbol{J}_{\mathrm{s}} + \boldsymbol{J}_{\mathrm{p}}\right)\dot{\boldsymbol{\omega}} + m_{\mathrm{s}}\hat{\boldsymbol{r}}_{\mathrm{s}}\dot{\boldsymbol{v}} + m_{\mathrm{p}}\dot{\hat{\boldsymbol{r}}}_{\mathrm{p}}\left(\boldsymbol{v} + \boldsymbol{\omega} \times \boldsymbol{r}_{\mathrm{p}} + \dot{\boldsymbol{r}}_{\mathrm{p}}\right) \\ & + m_{\mathrm{p}}\hat{\boldsymbol{r}}_{\mathrm{p}}\left(\dot{\boldsymbol{v}} + \dot{\boldsymbol{\omega}} \times \boldsymbol{r}_{\mathrm{p}} + \boldsymbol{\omega} \times \dot{\boldsymbol{r}}_{\mathrm{p}} + \ddot{\boldsymbol{r}}_{\mathrm{p}}\right) + \dot{\boldsymbol{J}}_{\mathrm{p}}\dot{\boldsymbol{\zeta}}_{\boldsymbol{b}} + \boldsymbol{J}_{\mathrm{p}}\ddot{\boldsymbol{\zeta}}_{\boldsymbol{b}}\end{aligned} \tag{A17}$$

Substituting Eqs. (A14) ~ (A17) into Eqs. (A9) and (A10), and reassigning these items, result in the final dynamics equations.

Appendix B:

$$\boldsymbol{A}(1,1) = \frac{\partial G_1}{\partial u} = \frac{1}{\left(m_{\mathrm{s}} + m_{\mathrm{p}} + \lambda_{11}\right)}\left(-\left(m_{\mathrm{p}}R_{\mathrm{p}} + m_{\mathrm{s}}r_{\mathrm{s3}}\right)\boldsymbol{A}(3,1) + \frac{\partial F_1}{\partial u}\right)$$

$$\boldsymbol{A}(1,2) = \frac{\partial G_1}{\partial w} = \frac{1}{\left(m_{\mathrm{s}} + m_{\mathrm{p}} + \lambda_{11}\right)}\left(-\left(m_{\mathrm{p}}R_{\mathrm{p}} + m_{\mathrm{s}}r_{\mathrm{s3}}\right)\boldsymbol{A}(3,2) + \frac{\partial F_1}{\partial w}\right)$$

$$\boldsymbol{A}(1,3) = \frac{\partial G_1}{\partial q} = \frac{1}{\left(m_{\mathrm{s}} + m_{\mathrm{p}} + \lambda_{11}\right)}\left(\left(-m_{\mathrm{s}} - m_{\mathrm{p}}\right)w_{\mathrm{d}} - \left(m_{\mathrm{p}}R_{\mathrm{p}} + m_{\mathrm{s}}r_{\mathrm{s3}}\right)\boldsymbol{A}(3,3)\right)$$

$$\boldsymbol{A}(1,4) = \frac{\partial G_1}{\partial \theta} = \frac{1}{\left(m_{\mathrm{s}} + m_{\mathrm{p}} + \lambda_{11}\right)}\left(-\left(m_{\mathrm{p}}R_{\mathrm{p}} + m_{\mathrm{s}}r_{\mathrm{s3}}\right)\boldsymbol{A}(3,4) + \frac{\partial F_1}{\partial \theta}\right)$$

$$\boldsymbol{A}(2,1) = \frac{\partial G_2}{\partial u} = \frac{1}{\left(m_{\mathrm{s}} + m_{\mathrm{p}} + \lambda_{33}\right)}\left(\left(m_{\mathrm{p}}r_{\mathrm{p1d}} + m_{\mathrm{s}}r_{\mathrm{s1}} - \lambda_{35}\right)\boldsymbol{A}(3,1) + \frac{\partial F_3}{\partial u}\right)$$

$$\boldsymbol{A}(2,2) = \frac{\partial G_2}{\partial w} = \frac{1}{\left(m_{\mathrm{s}} + m_{\mathrm{p}} + \lambda_{33}\right)}\left(\left(m_{\mathrm{p}}r_{\mathrm{p1d}} + m_{\mathrm{s}}r_{\mathrm{s1}} - \lambda_{35}\right)\boldsymbol{A}(3,2) + \frac{\partial F_3}{\partial w}\right)$$

$$\boldsymbol{A}(2,3) = \frac{\partial G_2}{\partial q} = \frac{1}{\left(m_{\mathrm{s}} + m_{\mathrm{p}} + \lambda_{33}\right)}\left(\left(m_{\mathrm{s}} + m_{\mathrm{p}}\right)u_{\mathrm{d}} + \left(m_{\mathrm{p}}r_{\mathrm{p1d}} + m_{\mathrm{s}}r_{\mathrm{s1}} - \lambda_{35}\right)\boldsymbol{A}(3,3)\right)$$

$$\boldsymbol{A}(2,4) = \frac{\partial G_2}{\partial \theta} = \frac{1}{\left(m_{\mathrm{s}} + m_{\mathrm{p}} + \lambda_{33}\right)}\left(\left(m_{\mathrm{p}}r_{\mathrm{p1d}} + m_{\mathrm{s}}r_{\mathrm{s1}} - \lambda_{35}\right)\boldsymbol{A}(3,4) + \frac{\partial F_3}{\partial \theta}\right)$$

$$\boldsymbol{A}(3,1) = \frac{\partial G_3}{\partial u} = \frac{1}{\left(J_{\mathrm{s22}} + J_{\mathrm{p22}}^{0} + m_{\mathrm{p}}R_{\mathrm{p}}^{\ 2} + m_{\mathrm{p}}r_{\mathrm{p1d}}^{\ 2} + \lambda_{55}\right)}\begin{pmatrix}-\left(m_{\mathrm{s}}r_{\mathrm{s3}} + m_{\mathrm{p}}R_{\mathrm{p}}\right)\boldsymbol{A}(1,1) \\ +\left(m_{\mathrm{p}}r_{\mathrm{p1d}} + m_{\mathrm{s}}r_{\mathrm{s1}} - \lambda_{53}\right)\boldsymbol{A}(2,1) + \dfrac{\partial T_2}{\partial u}\end{pmatrix}$$

$$\boldsymbol{A}(3,2) = \frac{\partial G_3}{\partial w} = \frac{1}{\left(J_{\mathrm{s22}} + J_{\mathrm{p22}}^{0} + m_{\mathrm{p}}R_{\mathrm{p}}^{\ 2} + m_{\mathrm{p}}r_{\mathrm{p1d}}^{\ 2} + \lambda_{55}\right)}\begin{pmatrix}-\left(m_{\mathrm{s}}r_{\mathrm{s3}} + m_{\mathrm{p}}R_{\mathrm{p}}\right)\boldsymbol{A}(1,2) \\ +\left(m_{\mathrm{p}}r_{\mathrm{p1d}} + m_{\mathrm{s}}r_{\mathrm{s1}} - \lambda_{53}\right)\boldsymbol{A}(2,2) + \dfrac{\partial T_2}{\partial w}\end{pmatrix}$$

$$\boldsymbol{A}(3,3)=\frac{\partial G_3}{\partial q}=\frac{1}{\left(J_{s22}+J_{p22}^0+m_pR_p{}^2+m_pr_{p1d}{}^2+\lambda_{55}\right)}\begin{pmatrix}\left(-m_pr_{p1d}-m_sr_{s1}\right)u_d+\left(-m_pR_p-m_sr_{s3}\right)w_d\\-\left(m_sr_{s3}+m_pR_p\right)\boldsymbol{A}(1,3)\\+\left(m_pr_{p1d}+m_sr_{s1}-\lambda_{53}\right)\boldsymbol{A}(2,3)+\dfrac{\partial T_2}{\partial q}\end{pmatrix}$$

$$\boldsymbol{A}(3,4)=\frac{\partial G_3}{\partial \theta}=\frac{1}{\left(J_{s22}+J_{p22}^0+m_pR_p{}^2+m_pr_{p1d}{}^2+\lambda_{55}\right)}\begin{pmatrix}-\left(m_sr_{s3}+m_pR_p\right)\boldsymbol{A}(1,4)\\+\left(m_pr_{p1d}+m_sr_{s1}-\lambda_{53}\right)\boldsymbol{A}(2,4)\\+\dfrac{\partial T_2}{\partial \theta}\end{pmatrix}$$

$$\boldsymbol{A}(4,3)=1$$

$$\boldsymbol{A}(4,1)=\boldsymbol{A}(4,2)=\boldsymbol{A}(4,4)=0$$

$$\boldsymbol{B}(1,1)=\frac{\partial G_1}{\partial r_{p1}}=\frac{1}{\left(m_s+m_p+\lambda_{11}\right)}\left(-\left(m_pR_p+m_sr_{s3}\right)\boldsymbol{B}(3,1)\right)$$

$$\boldsymbol{B}(1,2)=\frac{\partial G_1}{\partial m_b}=\frac{1}{\left(m_s+m_p+\lambda_{11}\right)}\left(-\left(m_pR_p+m_sr_{s3}\right)\boldsymbol{B}(3,2)+\frac{\partial F_1}{\partial m_b}\right)$$

$$\boldsymbol{B}(2,1)=\frac{\partial G_2}{\partial r_{p1}}=\frac{1}{\left(m_s+m_p+\lambda_{33}\right)}\left(m_pr_{p1d}+m_sr_{s1}-\lambda_{35}\right)\boldsymbol{B}(3,1)$$

$$\boldsymbol{B}(2,2)=\frac{\partial G_2}{\partial m_b}=\frac{1}{\left(m_s+m_p+\lambda_{33}\right)}\left(\left(m_pr_{p1d}+m_sr_{s1}-\lambda_{35}\right)\boldsymbol{B}(3,2)+\frac{\partial F_3}{\partial m_b}\right)$$

$$\boldsymbol{B}(3,1)=\frac{\partial G_3}{\partial r_{p1}}=-\frac{2m_pr_{p1d}}{\left(J_{s22}+J_{p22}^0+m_pR_p{}^2+m_pr_{p1d}{}^2+\lambda_{55}\right)^2}T_{2d}$$

$$+\frac{1}{\left(J_{s22}+J_{p22}^0+m_pR_p{}^2+m_pr_{p1d}{}^2+\lambda_{55}\right)}\begin{pmatrix}-\left(m_sr_{s3}+m_pR_p\right)\boldsymbol{B}(1,1)\\+\left(m_pr_{p1d}+m_sr_{s1}-\lambda_{53}\right)\boldsymbol{B}(2,1)+\dfrac{\partial T_2}{\partial r_{p1}}\end{pmatrix}$$

$$\boldsymbol{B}(3,2)=\frac{\partial G_3}{\partial m_b}=\frac{1}{\left(J_{s22}+J_{p22}^0+m_pR_p{}^2+m_pr_{p1d}{}^2+\lambda_{55}\right)}\begin{pmatrix}-\left(m_sr_{s3}+m_pR_p\right)\boldsymbol{B}(1,2)\\+\left(m_pr_{p1d}+m_sr_{s1}-\lambda_{53}\right)\boldsymbol{B}(2,2)\\\dfrac{\partial T_2}{\partial m_b}\end{pmatrix}$$

$$\boldsymbol{B}(4,1)=\boldsymbol{B}(4,2)=0$$

Let H_χ denote the partial differentiation operation as $\partial \mathrm{H}/\partial\chi|(\boldsymbol{x}_d, \boldsymbol{u}_d)$, then

$$T_{2d}=m_s g\left(-r_{s1}\cos\theta_d-r_{s3}\sin\theta_d\right)+m_p g\left(-r_{p1d}\cos\theta_d-R_p\sin\theta_d\right)-m_{bd}gr_{b1}\cos\theta_d+T_{DL2}$$

$$\frac{\partial F_1}{\partial u}=-D_u\cos\alpha_d+D\alpha_u\sin\alpha_d+L_u\sin\alpha_d+L\alpha_u\cos\alpha_d$$

$$\frac{\partial F_1}{\partial w}=-D_w\cos\alpha_d+D\alpha_w\sin\alpha_d+L_w\sin\alpha_d+L\alpha_w\cos\alpha_d$$

$$\frac{\partial F_1}{\partial \theta} = -m_{\mathrm{bd}} \mathrm{g} \cos\theta_{\mathrm{d}}$$

$$\frac{\partial F_1}{\partial m_{\mathrm{b}}} = -\mathrm{g} \sin\theta_{\mathrm{d}}$$

$$\frac{\partial F_3}{\partial u} = -L_u \cos\alpha_{\mathrm{d}} + L\alpha_u \sin\alpha_{\mathrm{d}} - D_u \sin\alpha_{\mathrm{d}} - D\alpha_u \cos\alpha_{\mathrm{d}}$$

$$\frac{\partial F_3}{\partial w} = -L_w \cos\alpha_{\mathrm{d}} + L\alpha_w \sin\alpha_{\mathrm{d}} - D_w \sin\alpha_{\mathrm{d}} - D\alpha_w \cos\alpha_{\mathrm{d}}$$

$$\frac{\partial F_3}{\partial \theta} = -m_{\mathrm{bd}} \mathrm{g} \sin\theta_{\mathrm{d}}$$

$$\frac{\partial F_3}{\partial m_{\mathrm{b}}} = \mathrm{g} \cos\theta_{\mathrm{d}}$$

$$\frac{\partial T_2}{\partial u} = T_{\mathrm{DL2}u}$$

$$\frac{\partial T_2}{\partial w} = T_{\mathrm{DL2}w}$$

$$\frac{\partial T_2}{\partial q} = T_{\mathrm{DL2}q}$$

$$\frac{\partial T_2}{\partial \theta} = m_{\mathrm{s}} \mathrm{g}\left(r_{\mathrm{s1}} \sin\theta_{\mathrm{d}} - r_{\mathrm{s3}} \cos\theta_{\mathrm{d}}\right) + m_{\mathrm{p}} \mathrm{g}\left(r_{\mathrm{p1d}} \sin\theta_{\mathrm{d}} - R_{\mathrm{p}} \cos\theta_{\mathrm{d}}\right) + m_{\mathrm{bd}} \mathrm{g} r_{\mathrm{b1}} \sin\theta_{\mathrm{d}}$$

$$\frac{\partial T_2}{\partial r_{\mathrm{p1}}} = -m_{\mathrm{p}} \mathrm{g} \cos\theta_{\mathrm{d}}$$

$$\frac{\partial T_2}{\partial m_{\mathrm{b}}} = -\mathrm{g} r_{\mathrm{b1}} \cos\theta_{\mathrm{d}}$$

where

$$\alpha_u = -\frac{w_{\mathrm{d}}}{{u_{\mathrm{d}}}^2 + {w_{\mathrm{d}}}^2}$$

$$\alpha_w = \frac{u_{\mathrm{d}}}{{u_{\mathrm{d}}}^2 + {w_{\mathrm{d}}}^2}$$

$$D_u = 2\left(K_{\mathrm{D0}} + K_{\mathrm{D}} \alpha_{\mathrm{d}}^2\right) u_{\mathrm{d}} - 2K_{\mathrm{D}} \alpha_{\mathrm{d}} w_{\mathrm{d}}$$

$$D_w = 2\left(K_{\mathrm{D0}} + K_{\mathrm{D}} \alpha_{\mathrm{d}}^2\right) w_{\mathrm{d}} + 2K_{\mathrm{D}} \alpha_{\mathrm{d}} u_{\mathrm{d}}$$

$$L_u = 2\left(K_{\mathrm{L0}} + K_{\mathrm{L}} \alpha_{\mathrm{d}}\right) u_{\mathrm{d}} - K_{\mathrm{L}} w_{\mathrm{d}}$$

$$L_w = 2\left(K_{\mathrm{L0}} + K_{\mathrm{L}} \alpha_{\mathrm{d}}\right) w_{\mathrm{d}} + K_{\mathrm{L}} u_{\mathrm{d}}$$

$$T_{\mathrm{DL2}u} = 2\left(K_{\mathrm{M0}} + K_{\mathrm{M}} \alpha_{\mathrm{d}}\right) u_{\mathrm{d}} - K_{\mathrm{M}} w_{\mathrm{d}}$$

$$T_{\mathrm{DL2}w} = 2\left(K_{\mathrm{M0}} + K_{\mathrm{M}} \alpha_{\mathrm{d}}\right) w_{\mathrm{d}} - K_{\mathrm{M}} u_{\mathrm{d}}$$

$$T_{\mathrm{DL2}q} = K_{\mathrm{q}} V_{\mathrm{d}}^2$$

Appendix C:

$$\boldsymbol{A}(1,1)=\frac{1}{\left(m_{\mathrm{s}}+m_{\mathrm{p}}\right)}\left(\left(m_{\mathrm{p}}R_{\mathrm{p}}+m_{\mathrm{s}}r_{\mathrm{s3}}\right)\boldsymbol{A}(2,1)-\left(m_{\mathrm{p}}r_{\mathrm{p1d}}+m_{\mathrm{s}}r_{\mathrm{s1}}\right)\boldsymbol{A}(3,1)+\frac{\partial F_2}{\partial v}\right)$$

$$\boldsymbol{A}(1,2)=\frac{1}{\left(m_{\mathrm{s}}+m_{\mathrm{p}}\right)}\begin{pmatrix}\left(m_{\mathrm{s}}+m_{\mathrm{p}}\right)w_{\mathrm{d}}\\+\left(m_{\mathrm{p}}R_{\mathrm{p}}+m_{\mathrm{s}}r_{\mathrm{s3}}\right)\boldsymbol{A}(2,2)\\-\left(m_{\mathrm{p}}r_{\mathrm{p1d}}+m_{\mathrm{s}}r_{\mathrm{s1}}\right)\boldsymbol{A}(3,2)\end{pmatrix}$$

$$\boldsymbol{A}(1,3)=\frac{1}{\left(m_{\mathrm{s}}+m_{\mathrm{p}}\right)}\begin{pmatrix}-\left(m_{\mathrm{s}}+m_{\mathrm{p}}\right)u_{\mathrm{d}}\\+\left(m_{\mathrm{p}}R_{\mathrm{p}}+m_{\mathrm{s}}r_{\mathrm{s3}}\right)\boldsymbol{A}(2,3)\\-\left(m_{\mathrm{p}}r_{\mathrm{p1d}}+m_{\mathrm{s}}r_{\mathrm{s1}}\right)\boldsymbol{A}(3,3)\end{pmatrix}$$

$$\boldsymbol{A}(1,4)=\frac{1}{\left(m_{\mathrm{s}}+m_{\mathrm{p}}\right)}\begin{pmatrix}\left(m_{\mathrm{p}}R_{\mathrm{p}}+m_{\mathrm{s}}r_{\mathrm{s3}}\right)\boldsymbol{A}(2,4)\\-\left(m_{\mathrm{p}}r_{\mathrm{p1d}}+m_{\mathrm{s}}r_{\mathrm{s1}}\right)\boldsymbol{A}(3,4)+\frac{\partial F_2}{\partial \varphi}\end{pmatrix}$$

$$\boldsymbol{A}(1,5)=\frac{1}{\left(m_{\mathrm{s}}+m_{\mathrm{p}}\right)}\begin{pmatrix}\left(m_{\mathrm{p}}R_{\mathrm{p}}+m_{\mathrm{s}}r_{\mathrm{s3}}\right)\boldsymbol{A}(2,5)\\-\left(m_{\mathrm{p}}r_{\mathrm{p1d}}+m_{\mathrm{s}}r_{\mathrm{s1}}\right)\boldsymbol{A}(3,5)\end{pmatrix}$$

$$\boldsymbol{A}(2,1)=\frac{1}{\left(J_{\mathrm{s11}}+J_{\mathrm{p11}}^{0}+m_{\mathrm{p}}R_{\mathrm{p}}{}^{2}\right)}\begin{pmatrix}\left(m_{\mathrm{p}}R_{\mathrm{p}}+m_{\mathrm{s}}r_{\mathrm{s3}}\right)\boldsymbol{A}(1,1)\\-\left(J_{\mathrm{s13}}-m_{\mathrm{p}}R_{\mathrm{p}}r_{\mathrm{p1d}}\right)\boldsymbol{A}(3,1)+\frac{\partial T_1}{\partial v}\end{pmatrix}$$

$$\boldsymbol{A}(2,2)=\frac{1}{\left(J_{\mathrm{s11}}+J_{\mathrm{p11}}^{0}+m_{\mathrm{p}}R_{\mathrm{p}}{}^{2}\right)}\begin{pmatrix}-\left(m_{\mathrm{s}}r_{\mathrm{s3}}+m_{\mathrm{p}}R_{\mathrm{p}}\right)w_{\mathrm{d}}+\left(m_{\mathrm{p}}R_{\mathrm{p}}+m_{\mathrm{s}}r_{\mathrm{s3}}\right)\boldsymbol{A}(1,2)\\-\left(J_{\mathrm{s13}}-m_{\mathrm{p}}R_{\mathrm{p}}r_{\mathrm{p1d}}\right)\boldsymbol{A}(3,2)+\frac{\partial T_1}{\partial p}\end{pmatrix}$$

$$\boldsymbol{A}(2,3)=\frac{1}{\left(J_{\mathrm{s11}}+J_{\mathrm{p11}}^{0}+m_{\mathrm{p}}R_{\mathrm{p}}{}^{2}\right)}\begin{pmatrix}m_{\mathrm{s}}r_{\mathrm{s3}}u_{\mathrm{d}}+\left(m_{\mathrm{p}}R_{\mathrm{p}}+m_{\mathrm{s}}r_{\mathrm{s3}}\right)\boldsymbol{A}(1,3)\\-\left(J_{\mathrm{s13}}-m_{\mathrm{p}}R_{\mathrm{p}}r_{\mathrm{p1d}}\right)\boldsymbol{A}(3,3)+\frac{\partial T_1}{\partial r}\end{pmatrix}$$

$$\boldsymbol{A}(2,4)=\frac{1}{\left(J_{\mathrm{s11}}+J_{\mathrm{p11}}^{0}+m_{\mathrm{p}}R_{\mathrm{p}}{}^{2}\right)}\begin{pmatrix}\left(m_{\mathrm{p}}R_{\mathrm{p}}+m_{\mathrm{s}}r_{\mathrm{s3}}\right)\boldsymbol{A}(1,4)\\-\left(J_{\mathrm{s13}}-m_{\mathrm{p}}R_{\mathrm{p}}r_{\mathrm{p1d}}\right)\boldsymbol{A}(3,4)+\frac{\partial T_1}{\partial \varphi}\end{pmatrix}$$

$$\boldsymbol{A}(2,5)=\frac{1}{\left(J_{\mathrm{s11}}+J_{\mathrm{p11}}^{0}+m_{\mathrm{p}}R_{\mathrm{p}}{}^{2}\right)}\begin{pmatrix}\left(m_{\mathrm{p}}R_{\mathrm{p}}+m_{\mathrm{s}}r_{\mathrm{s3}}\right)\boldsymbol{A}(1,5)\\-\left(J_{\mathrm{s13}}-m_{\mathrm{p}}R_{\mathrm{p}}r_{\mathrm{p1d}}\right)\boldsymbol{A}(3,5)\end{pmatrix}$$

$$\boldsymbol{A}(3,1)=\frac{1}{\left(J_{\mathrm{s33}}+J_{\mathrm{p33}}^{0}+m_{\mathrm{p}}r_{\mathrm{p1d}}{}^{2}\right)}\left(-\left(m_{\mathrm{p}}r_{\mathrm{p1d}}+m_{\mathrm{s}}r_{\mathrm{s1}}\right)\boldsymbol{A}(1,1)-\left(J_{\mathrm{s31}}-m_{\mathrm{p}}R_{\mathrm{p}}r_{\mathrm{p1d}}\right)\boldsymbol{A}(2,1)+\frac{\partial T_3}{\partial v}\right)$$

$$\boldsymbol{A}(3,2)=\frac{1}{\left(J_{\mathrm{s33}}+J_{\mathrm{p33}}^{0}+m_{\mathrm{p}}r_{\mathrm{p1d}}{}^{2}\right)}\begin{pmatrix}\left(m_{\mathrm{s}}r_{\mathrm{s1}}+m_{\mathrm{p}}r_{\mathrm{p1d}}\right)w_{\mathrm{d}}-\left(m_{\mathrm{p}}r_{\mathrm{p1d}}+m_{\mathrm{s}}r_{\mathrm{s1}}\right)\boldsymbol{A}(1,2)\\-\left(J_{\mathrm{s31}}-m_{\mathrm{p}}R_{\mathrm{p}}r_{\mathrm{p1d}}\right)\boldsymbol{A}(2,2)+\frac{\partial T_3}{\partial p}\end{pmatrix}$$

$$\boldsymbol{A}(3,3)=\frac{1}{\left(J_{s33}+J_{p33}^{0}+m_{p}r_{p1d}{}^{2}\right)}\begin{pmatrix}-\left(m_{s}r_{s1}+m_{p}r_{p1d}\right)u_{d}-\left(m_{p}r_{p1d}+m_{s}r_{s1}\right)\boldsymbol{A}(1,3)\\-\left(J_{s31}-m_{p}R_{p}r_{p1d}\right)\boldsymbol{A}(2,3)+\dfrac{\partial T_{3}}{\partial r}\end{pmatrix}$$

$$\boldsymbol{A}(3,4)=\frac{1}{\left(J_{s33}+J_{p33}^{0}+m_{p}r_{p1d}{}^{2}\right)}\left(-\left(m_{p}r_{p1d}+m_{s}r_{s1}\right)\boldsymbol{A}(1,4)-\left(J_{s31}-m_{p}R_{p}r_{p1d}\right)\boldsymbol{A}(2,4)+\frac{\partial T_{3}}{\partial\varphi}\right)$$

$$\boldsymbol{A}(3,5)=\frac{1}{\left(J_{s33}+J_{p33}^{0}+m_{p}r_{p1d}{}^{2}\right)}\begin{pmatrix}-\left(m_{p}r_{p1d}+m_{s}r_{s1}\right)\boldsymbol{A}(1,5)\\-\left(J_{s31}-m_{p}R_{p}r_{p1d}\right)\boldsymbol{A}(2,5)\end{pmatrix}$$

$$\boldsymbol{A}(4,1)=0$$

$$\boldsymbol{A}(4,2)=1$$

$$\boldsymbol{A}(4,3)=\tan\theta_{d}$$

$$\boldsymbol{A}(4,4)=0$$

$$\boldsymbol{A}(4,5)=0$$

$$\boldsymbol{A}(5,1)=0$$

$$\boldsymbol{A}(5,2)=0$$

$$\boldsymbol{A}(5,3)=\sec\theta_{d}$$

$$\boldsymbol{A}(5,4)=0$$

$$\boldsymbol{A}(5,5)=0$$

$$\boldsymbol{B}(1,1)=\frac{1}{\left(m_{s}+m_{p}\right)}\begin{pmatrix}\left(m_{p}R_{p}+m_{s}r_{s3}\right)\boldsymbol{B}(2,1)\\-\left(m_{p}r_{p1d}+m_{s}r_{s1}\right)\boldsymbol{B}(3,1)\end{pmatrix}$$

$$\boldsymbol{B}(2,1)=\frac{1}{\left(J_{s11}+J_{p11}^{0}+m_{p}R_{p}{}^{2}\right)}\begin{pmatrix}\left(m_{p}R_{p}+m_{s}r_{s3}\right)\boldsymbol{B}(1,1)\\-\left(J_{s13}-m_{p}R_{p}r_{p1d}\right)\boldsymbol{B}(3,1)+\dfrac{\partial T_{1}}{\partial\zeta}\end{pmatrix}$$

$$\boldsymbol{B}(3,1)=\frac{1}{\left(J_{s33}+J_{p33}^{0}+m_{p}r_{p1d}{}^{2}\right)}\begin{pmatrix}-\left(m_{p}r_{p1}+m_{s}r_{s1}\right)\boldsymbol{B}(1,1)\\-\left(J_{s31}-m_{p}R_{p}r_{p1d}\right)\boldsymbol{B}(2,1)+\dfrac{\partial T_{3}}{\partial\zeta}\end{pmatrix}$$

$$\boldsymbol{B}(4,1)=0$$

$$\boldsymbol{B}(5,1)=0$$

where

$$\frac{\partial F_{2}}{\partial v}=SF_{v}-D\beta_{v}$$

$$\frac{\partial F_{2}}{\partial\varphi}=m_{bd}\mathrm{g}\cos\theta_{d}$$

$$\frac{\partial T_{1}}{\partial v}=\cos\alpha_{d}\left(T_{DL1v}-T_{DL2}\beta_{v}\right)-T_{DL3v}\sin\alpha_{d}$$

$$\frac{\partial T_{1}}{\partial p}=T_{DL1p}\cos\alpha_{d}$$

$$\frac{\partial T_1}{\partial r} = -T_{\mathrm{DL3}r}\sin\alpha_{\mathrm{d}}$$

$$\frac{\partial T_1}{\partial \varphi} = -m_{\mathrm{s}}\mathrm{g}r_{\mathrm{s}3}\cos\theta_{\mathrm{d}} - m_{\mathrm{p}}\mathrm{g}R_{\mathrm{p}}\cos\theta_{\mathrm{d}}$$

$$\frac{\partial T_3}{\partial v} = \sin\alpha_{\mathrm{d}}\left(T_{\mathrm{DL1}v} - T_{\mathrm{DL2}}\beta_v\right) + T_{\mathrm{DL3}v}\cos\alpha_{\mathrm{d}}$$

$$\frac{\partial T_3}{\partial p} = T_{\mathrm{DL1}p}\sin\alpha_{\mathrm{d}}$$

$$\frac{\partial T_3}{\partial r} = T_{\mathrm{DL3}r}\cos\alpha_{\mathrm{d}}$$

$$\frac{\partial T_3}{\partial \varphi} = \left(m_{\mathrm{s}}r_{\mathrm{s}1} + m_{\mathrm{p}}r_{\mathrm{p1d}} + m_{\mathrm{bd}}r_{\mathrm{b}1}\right)\mathrm{g}\cos\theta_{\mathrm{d}}$$

$$\frac{\partial T_1}{\partial \zeta} = -m_{\mathrm{p}}\mathrm{g}R_{\mathrm{p}}\cos\theta_{\mathrm{d}}$$

$$\frac{\partial T_3}{\partial \zeta} = -m_{\mathrm{p}}\mathrm{g}R_{\mathrm{p}}\sin\theta_{\mathrm{d}}$$

$$\beta_v = \frac{1}{\sqrt{{u_{\mathrm{d}}}^2 + {w_{\mathrm{d}}}^2}}$$

$$SF_v = {V_{\mathrm{d}}}^2 K_\beta \beta_v$$

$$T_{\mathrm{DL1}v} = {V_{\mathrm{d}}}^2 K_{\mathrm{MR}}\beta_v$$

$$T_{\mathrm{DL3}v} = {V_{\mathrm{d}}}^2 K_{\mathrm{MY}}\beta_v$$

$$T_{\mathrm{DL1}p} = {V_{\mathrm{d}}}^2 K_{\mathrm{p}}$$

$$T_{\mathrm{DL3}r} = {V_{\mathrm{d}}}^2 K_{\mathrm{r}}$$

Appendix D: Parameters and coefficients in simulations

Table D-1 Mass and geometric characteristic parameters of Petrel-II glider (Wu et al., 2021b; Yang et al., 2017)

Parameter	Value
m_{s}	54.5 kg
r_{s}	[-0.0271, 0, 0.0199] $^{\mathrm{T}}$ m
$\boldsymbol{J}_{\mathrm{s}}$	$\begin{bmatrix} 0.5550 & 0 & 0.1246 \\ 0 & 18.5456 & 0 \\ 0.1246 & 0 & 18.4706 \end{bmatrix}$ kg·m^2
$r_{\mathrm{b}1}$	0.9 m
m_{p}	16.4 kg
R_{p}	0.016 m
$\boldsymbol{J}_{\mathrm{p}}^{0}$	*diag*[0.03, 0.17, 0.18] kg·m^2
K_{vh}	0.27172 mL/m

Table D-2 Inertial hydrodynamic coefficients of Petrel-II glider (Wu et al., 2021b)

Coefficient	Value	Coefficient	Value
λ_{11}	1.30 kg	λ_{55}	23.56 kg·m^2
λ_{22}	60.53 kg	λ_{66}	21.83 kg·m^2
λ_{33}	79.66 kg	$\lambda_{26}=\lambda_{62}$	-19.35 kg·m
λ_{44}	0 kg·m^2	$\lambda_{35}=\lambda_{53}$	12.37 kg·m

Table D-3 Viscous hydrodynamic coefficients of Petrel-II glider (Wu et al., 2021b)

Coefficient	Value	Coefficient	Value
K_{D0}	7.65 kg/m	K_{p}	-18.98 kg·s/rad
K_{D}	357.97 kg/m/rad^2	K_{M0}	0.3 kg
K_{β}	-100.13 kg/m/rad	K_{M}	-61.02 kg/rad
K_{L0}	-0.5 kg/m	K_{q}	-196.78 kg·s/rad
K_{L}	381.73 kg/m/rad	K_{MY}	32.63 kg/rad
K_{MR}	-55.81 kg/rad	K_{r}	-372.54 kg·s/rad

Table D-4 Water density gradient parameters (Yang et al., 2017)

Parameter	Value	Parameter	Value
p_1	-5.083×10^{-12} kg/m^7	p_4	0.02248 kg/m^4
p_2	1.95×10^{-8} kg/m^6	p_5	1022.7 kg/m^3
p_3	-2.75×10^{-5} kg/m^5		